

---

# UNiTE: Unitary N-body Tensor Equivariant Network with Applications to Quantum Chemistry

---

**Zhuoran Qiao**  
California Institute of Technology  
zqiao@caltech.edu

**Anders S. Christensen**  
Entos, Inc.  
anders@entos.ai

**Matthew Welborn**  
Entos, Inc.  
matt@entos.ai

**Frederick R. Manby**  
Entos, Inc.  
fred@entos.ai

**Anima Anandkumar**  
California Institute of Technology  
NVIDIA  
anima@caltech.edu

**Thomas F. Miller III**  
California Institute of Technology  
Entos, Inc.  
tfm@caltech.edu

## Abstract

Equivariant neural networks have been successful in incorporating various types of symmetries, but are mostly limited to vector representations of geometric objects. Despite the prevalence of higher-order tensors in various application domains, e.g. in quantum chemistry, equivariant neural networks for general tensors remain underexplored. Previous strategies for learning equivariant functions on tensors mostly rely on expensive tensor factorization which is not scalable when the dimensionality of the problem becomes large. In this work, we propose unitary  $N$ -body tensor equivariant neural network (UNiTE), an architecture for a general class of symmetric tensors called  $N$ -body tensors. The proposed neural network is equivariant with respect to the actions of a unitary group, such as the group of 3D rotations. Furthermore, it has a linear time complexity with respect to the number of non-zero elements in the tensor. When applied to quantum chemistry, UNiTE in combination with a low-cost physics-based molecular representation outperforms state-of-the-art machine learning methods on multiple benchmarks. Finally, we show that UNiTE achieves a robust zero-shot generalization performance on diverse downstream chemistry tasks, while being three orders of magnitude faster than conventional numerical methods with competitive accuracy.

## 1 Introduction

Geometric deep learning is focused on building neural network models for geometric objects, and it needs to encode the symmetries present in the problem domain [1]. A geometric object is usually represented using a reference frame input to the neural network model. Symmetries are incorporated via the concept of *equivariance* defined as the property of being independent of the choice of reference frame.

One intuitive and common way to encode a geometric object is to represent it as the positions of a collection of points, i.e. a set of vectors. Examples include point clouds [2], grids [3] and meshes [4]. Many previous geometric learning methods, termed *equivariant neural networks*, have been designed by considering how the vectors transform under symmetry operations on the reference frames. These equivariant neural networks have successfully ‘baked’ symmetries into deep neural networks in various application domains, such as autonomous driving [5] and molecular design [6].

However, we identify two remaining challenges that are not addressed in prior works:

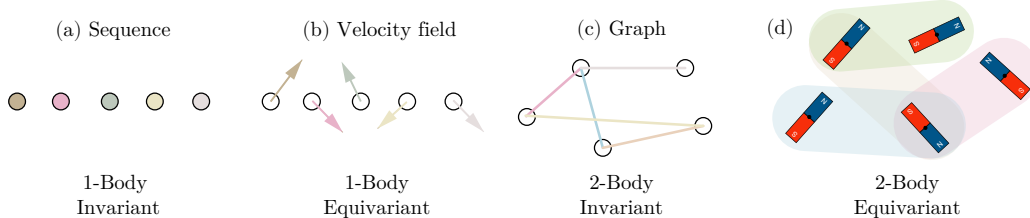


Figure 1: Examples of  $N$ -body tensors.

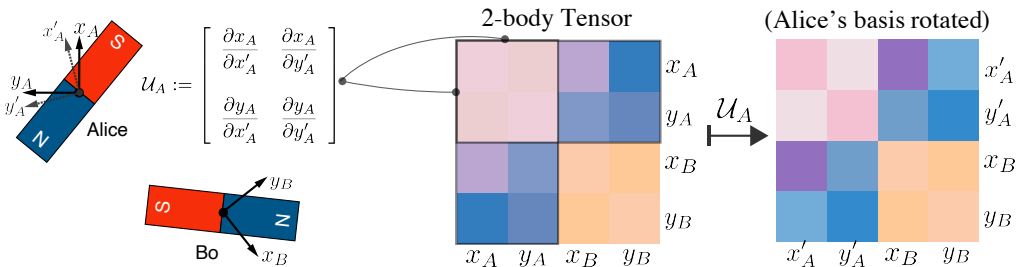


Figure 2: Illustrating an  $N$ -body tensor with  $N = 2$ . Imagine Alice and Bo are doing experiments with two bar magnets without knowing each other’s reference frame. The magnetic interactions depend on both bar magnets’ orientations and can be written as a 2-body tensor. When Alice make a rotation on her reference frame, sub-tensors containing index  $A$  are transformed by a unitary matrix  $\mathcal{U}_A$ , giving rise to the 2-body tensor coefficients in the transformed basis. We design neural network to be equivariant to all such local basis transformations.

- (a) Prior works mostly focus on vector (i.e. order-1 tensor) representations of a geometric entity, but constructing equivariant neural networks for general tensors is largely unexplored;
- (b) They are often specific to one form of data (e.g., point clouds or grids) or one class of groups, while lacking a more generic framework.

Higher-order tensors are ubiquitous, and many famous problems in physical science, e.g. general relativity, are defined using tensors of order larger than one. However, it is challenging to directly apply equivariant neural networks for learning on those tensors. First, the order of learning targets of interest, mostly scalars (order-0) or vectors (order-1), usually differ from the order of input tensors and cannot be handled in those frameworks. Second, many equivariant neural networks rely on computing tensor products of vectors and their decompositions in the neural network building blocks [2, 7], which is not applicable to cases where the inputs are tensors. A few works designed for learning equivariant functions on tensors in specific domains rely on tensor factorization [8], which is not scalable when the order of tensors or the dimension of the physical spaces become large.

The absence of a more generic framework may limit their applicability when symmetries in the learning problem become more complicated. For example, in particle physics, each particle is linked with a different symmetry group [9]. Without a unified approach one has to exhaustively formulate equivariant neural networks for every instance of such systems.

In this work, we are interested in general tensors that encode *relations* among multiple geometric objects. We define a class of tensors  $\mathbf{T}$ , which we call  *$N$ -body tensors*, that can describe such  $N$ -object relations. Many forms of data can be interpreted as examples of  $N$ -body tensors (Figure 1). For example, sequences are scalar-valued features concatenated together to form a flattened array which is an order-1 tensor (e.g. word embeddings). They do not contain any positional information in physical space, therefore their values are trivially unchanged when rotating the reference frame. Thus sequences are classified as 1-body invariant tensors. Velocity fields can be understood as sequences with an extra directional information. When rotating the reference frame, the values recorded on  $xyz$ -components of each sub-vector changes equivariantly. therefore velocity fields are interpreted as

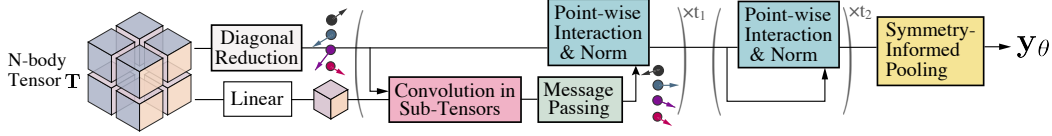


Figure 3: The UNiTE model architecture. UNiTE first initialize order-1 (vector) representations via a diagonal sub-tensor reduction layer (Section 4.2), then updates representations through convolution, message-passing (Section 4.1), and point-wise interaction blocks with Equivariant Normalization (Section 4.3). A symmetry-informed pooling is used at the end to readout the predictions  $\mathbf{y}_\theta$ .

1-body equivariant tensors. Graphs encode relational information between a set of nodes, defined by their adjacency matrices (order-2 tensors). Since the adjacency matrix of a graph only contains scalar values, graphs are also rotation-invariant and are 2-body invariant tensors.

To further motivate towards the general  $N$ -body case, we can consider a toy model where many bar magnets are placed on a table (Figure 1d). The magnetic interaction between a pair of bar magnets (say, Alice and Bo) in fact cannot be simply expressed by the magnets’ orientation vectors, but need to be written as a  $2 \times 2$  matrix dependent on Alice’s and Bo’s reference frames. Values on the matrix are rotationally-equivariant because it columns and rows are transformed by a rotation matrix as Alice or Bo rotates their reference frames (Figure 2); hence, this is an example of 2-body equivariant tensor. Given  $M$  bar magnets, the 2-body tensor representing the system depicted in Figure 1d is thus a  $(2M \times 2M)$  square matrix stacked from such  $2 \times 2$  matrices, which may be also viewed as a graph of those order-2 sub-tensors (matrices).

We propose UNiTE for the general case of  $N$ -body equivariant tensors where both  $N$ -object relations and physical-space information are present. **Our contributions are:**

- We present Unitary  $N$ -body Tensor Equivariant neural network (UNiTE), a novel architecture for  $N$ -body tensors of any  $N$  in arbitrary-dimensional physical spaces. It is equivariant with respect to unitary transformations on the reference frames and tensor index permutations.
- The proposed approach realizes equivariance without requiring explicit tensor factorization operations. It is efficient, having a linear time complexity with respect to the number of non-zero elements in the tensor.
- Generalization and training stability of equivariant neural networks is improved using a simple but effective normalization scheme, Equivariant Normalization (EvNorm), proposed in this paper.

UNiTE has a modular architecture (Figure 3) that updates a set of latent order-1 (i.e. vectors) representations:  $\mathbf{h}^{t=0} \mapsto \mathbf{h}^{t=1} \mapsto \dots \mapsto \mathbf{h}^{t=t_f}$  and performs pooling at the end. The vector representations are defined on each geometric object  $\mathbf{h}^t := [\mathbf{h}_1^t, \mathbf{h}_2^t, \dots, \mathbf{h}_d^t]$ .

The initial vector representations  $\mathbf{h}^{t=0}$  are generated by decomposing diagonal sub-tensors of the  $N$ -body tensor into vectors without explicitly solving tensor factorization, based on a theoretical result in this work which is connected to the Wigner-Eckart Theorem in quantum physics [10]. We now give some intuitive explanations for our theoretical results: the diagonal sub-tensors can be viewed as isolated systems because they can be modeled as being infinitely apart and only interacting with an external field. The Wigner-Eckart Theorem describes rotational symmetry for such isolated systems, and we generalize it to  $N$ -body tensors in our work.

Each update step  $\mathbf{h}^t \mapsto \mathbf{h}^{t+1}$  is composed of (a) Convolution, (b) Message passing, and (c) Point-wise interaction blocks. All such blocks are designed to be equivariant with respect to index permutations and both global and local reference-frame transformations, by (a) contracting the  $N$ -body tensor with vector representations  $\mathbf{h}^t$  to make the contracted tensor dimensions invariant to reference-frame transformations, and (b) designing neural network layers on  $\mathbf{h}^t$  that preserve its transformation rule under rotations and reflections. Thus, we have an end-to-end equivariant neural network.

In an update step  $\mathbf{h}^t \mapsto \mathbf{h}^{t+1}$ , each sub-tensor of the  $N$ -body tensor input  $\mathbf{T}$  is first contracted with products of the vector representations  $\mathbf{h}^t$ . This tensor contraction operation can be interpreted as performing an  $(N - 1)$  dimensional convolution using the sub-tensors of  $\mathbf{T}$  as convolution kernels, therefore we call it *convolution-in-sub-tensors* block. The convolution outputs from each sub-tensor

is an order-1 tensor (i.e. vectors); those convolution outputs are then passed into a *message-passing* block, which is analogous to a message-passing operation on edges in graph neural networks (GNNs) but are performed on edges connecting  $N$  nodes. The outputs are then fed into a *point-wise interaction* block with the previous-step representation  $\mathbf{h}^t$  to complete the update  $\mathbf{h}^t \mapsto \mathbf{h}^{t+1}$ . The point-wise interaction blocks are constructed as a stack of multi-layer perceptrons (MLPs), vector outer-products and skip connections. Within those blocks, a *matching layer* is used to ‘glue’ the basis of  $\mathbf{h}^t$  with the basis used to define the tensor  $\mathbf{T}$ . Presence of the matching layer ensures equivariance is maintained.

In addition, we propose a novel normalization layer, Equivariant Normalization (EvNorm). EvNorm normalizes the scales of vectors in the order-1 (i.e. vectors) representation, while recording those vectors’ directional information to be recovered after normalization. Therefore it performs normalization without sacrificing model equivariance. EvNorm can be feasibly integrated within a point-wise interaction block through first applying EvNorm on the input vector representations, then using an MLP to the array of normalized vector scales, and finally multiplying the vector directions recorded by EvNorm to the MLP’s output. In practice, we found using EvNorm within the point-wise interaction blocks greatly stabilizes training, improves model generalization, and eliminates the need for hand-tuning weight initializations and learning rates across different tasks.

In UNiTE, the only operation explicitly performed on the tensor input is the  $(N - 1)$  dimensional convolution, which has a linear time complexity with respect to the number of non-zero elements in the  $N$ -body tensor. The scalability of the architecture with respect to the number of physical interactions in the learning task is therefore ensured.

**Quantum chemistry with UNiTE.** One main motivation for us to develop UNiTE is to enable learning quantum chemistry properties based on 2-body and higher-order tensor representations of molecules. Such  $N$ -body tensor molecular representations are necessary to encode the interactions between electrons and atoms, since their motions are quantum-mechanical and are described by high-dimensional functions. Furthermore, the chemical properties predicted by the model need to satisfy their symmetry constraints. When applied to quantum chemistry, empirically we find UNiTE in combination with a tight-binding quantum-mechanical-approximation-based molecular representation showing superior performance over all existing machine learning approaches for that domain which were only capable of utilizing molecular geometry inputs. In addition, it outperforms previous method that uses the same physics-based molecular representation by 45% for learning molecule formation energies on QM9.

Beyond data efficiency on benchmarks in train-test split settings, a more practical and challenging aspect is whether the neural network can deduce down-stream properties of humans’ interest once being trained on primitive physical quantities. This aspect is even more critical in the domain of quantum chemistry, where all chemical reactions are fundamentally related to the energies of molecules through the famous Schrödinger equation, but directly obtaining down-stream properties about chemical reactions by solving the Schrödinger equation is both theoretically and computationally prohibitive. In this work, we find UNiTE model pre-trained on energies of 236k molecules achieves robust performance on various practical, down stream chemistry tasks without any model fine-tuning. Even in such a zero-shot setting, it offers an accuracy similar or better than conventional numerical methods with up to **3-orders-of-magnitude** speedup.

## 2 Related works

**Equivariant neural networks.** Equivariant neural networks were first introduced for homogeneous grid and point cloud data[2, 3, 7, 11], and have been generalized to symmetries on non-Euclidean manifolds[4, 12, 13]. While being powerful, those architectures are typically designed based on order-1 tensors in the geometry. In contrast, our goal is to develop equivariant neural network operating on a  $N$ -body tensors for geometric data that may entail higher-order relational information.

**Graph neural networks.** Graph neural networks (GNNs) are gaining popularity for learning on relational data [14, 15]. They are permutation-equivariant with respect to reordering the node indices in the graph. Recent works have extended graph neural networks to hyper-graphs [16, 17], as well as to equivariance under continuous symmetry transformations [11, 18] when the set of nodes in the graph correspond to point clouds in the Euclidean space. GNNs on point clouds primarily focused on the global 3D rotational symmetry, and achieve rotation-equivariance using either a set of harmonic

basis functions [2, 19] or the simpler standard basis [18, 20]. Some GNNs have also been developed with special interests in N-body physical simulation data or quantum chemistry [19–26].

**Equivariance for order- $N$  tensors.** To our best knowledge, closest to ours in spirit is a pair of recent works [8, 27] developed for a special class of order-2  $SU(n)$  tensors in a high-energy physics problem. They proposed to apply learnable equivariant transformations on those order-2 tensors through eigen-decomposition, with a symmetrization algorithm eigenvalues to enforce permutation equivariance. But in a general order- $N$  setting, such an approach requires performing tensor factorization for each order- $N$  sub-tensor, which would introduce significant computational costs and can be intractable when  $N$  or  $n$  become large.

### 3 $N$ -body tensors

We are interested in a class of tensors  $\mathbf{T}$ , for which each sub-tensor  $\mathbf{T}(u_1, u_2, \dots, u_N)$  describes relation among a collection of  $N$  geometric objects defined in an  $n$ -dimensional physical space. For simplicity, we will introduce the tensors of interest using a special case based on point clouds embedded in the  $n$ -dimensional Euclidean space, associating a (possibly different) set of orthogonal basis with each point’s neighbourhood. In this setting, our main focus is the change of the order- $N$  tensor’s coefficients when applying  $n$ -dimensional rotations and reflections to the local reference frames. Our proposed approach can be generalized to non-flat manifolds, harmonic basis and complex fields, and a general problem statement will be provided in Appendix A.

**Definition 1 ( $N$ -body tensor).** Let  $\{\mathbf{x}_1, \mathbf{x}_2, \dots, \mathbf{x}_d\}$  be  $d$  points in  $\mathbb{R}^n$  for each  $u \in \{1, 2, \dots, d\}$ . For each point index  $u$ , we define an orthonormal basis (local reference frame)  $\{\mathbf{e}_{u;v_u}\}$  centered at  $\mathbf{x}_u$ <sup>1</sup>, and denote the space spanned by the basis as  $V_u := \text{span}(\{\mathbf{e}_{u;v_u}\}) \subseteq \mathbb{R}^n$ . We consider a tensor  $\hat{\mathbf{T}}$  defined via  $N$ -th direct products of the ‘concatenated’ basis  $\{\mathbf{e}_{u;v_u}; (u, v_u)\}$ :

$$\hat{\mathbf{T}} := \sum_{\vec{u}, \vec{v}} T((u_1; v_1), (u_2; v_2), \dots, (u_N; v_N)) \mathbf{e}_{u_1;v_1} \otimes \mathbf{e}_{u_2;v_2} \otimes \dots \otimes \mathbf{e}_{u_N;v_N} \quad (1)$$

$\hat{\mathbf{T}}$  is a tensor of order- $N$  and is an element of  $(\bigoplus_{u=1}^d V_u)^{\otimes N}$ . We call its coefficients  $\mathbf{T}$  an  $N$ -body tensor if  $\mathbf{T}$  is invariant to global translations ( $\forall \mathbf{x}_0 \in \mathbb{R}^n, \mathbf{T}[\mathbf{x}] = \mathbf{T}[\mathbf{x} + \mathbf{x}_0]$ ), and is symmetric:

$$T((u_1; v_1), (u_2; v_2), \dots, (u_N; v_N)) = T((u_{\sigma_1}; v_{\sigma_1}), (u_{\sigma_2}; v_{\sigma_2}), \dots, (u_{\sigma_N}; v_{\sigma_N})) \quad (2)$$

where  $\sigma$  denotes arbitrary permutation on its dimensions  $\{1, 2, \dots, N\}$ . Note that each sub-tensor,  $\mathbf{T}_{\vec{u}}$ , does not have to be symmetric. The shorthand notation  $\vec{u} := (u_1, u_2, \dots, u_N)$  indicates a subset of  $N$  points in  $\{\mathbf{x}_1, \mathbf{x}_2, \dots, \mathbf{x}_d\}$  which then identifies a sub-tensor<sup>2</sup>  $\mathbf{T}_{\vec{u}} := \mathbf{T}(u_1, u_2, \dots, u_N)$  in the  $N$ -body tensor  $\mathbf{T}$ ;  $\vec{v} := (v_1, v_2, \dots, v_N)$  index a coefficient  $T_{\vec{u}}(v_1, v_2, \dots, v_N) := T((u_1; v_1), (u_2; v_2), \dots, (u_N; v_N))$  in a sub-tensor  $\mathbf{T}_{\vec{u}}$ , where each index  $v_j \in \{1, 2, \dots, \dim(V_{u_j})\}$  for  $j \in \{1, 2, \dots, N\}$ .

We aim to build neural networks  $\hat{\mathcal{F}}_\theta : (\bigoplus_{u=1}^d V_u)^{\otimes N} \rightarrow \mathcal{Y}$  that map  $\hat{\mathbf{T}}$  to order-1 tensor- or scalar-valued outputs  $\mathbf{y} \in \mathcal{Y}$ . While  $\hat{\mathbf{T}}$  is independent of the choice of local reference frame  $\mathbf{e}_u$ , its coefficients  $\mathbf{T}$  (i.e. the  $N$ -body tensor) vary when rotating or reflecting the basis  $\mathbf{e}_u := \{\mathbf{e}_{u;v_u}; v_u\}$ , i.e. acted by an element  $\mathcal{U}_u \in O(n)$ . Therefore, the neural network  $\hat{\mathcal{F}}_\theta$  should be constructed equivariant with respect to those reference frame transformations.

**Equivariance.** For a map  $f : \mathcal{V} \rightarrow \mathcal{Y}$  and a group  $G$ ,  $f$  is said to be  $G$ -equivariant if for all  $g \in G$  and  $\mathbf{v} \in \mathcal{V}$ ,  $g \cdot f(\mathbf{v}) = f(g \cdot \mathbf{v})$ . In our case, the group  $G$  is composed of (a) Unitary transformations  $\mathcal{U}_u$  locally applied to basis:  $\mathbf{e}_u \mapsto \mathcal{U}_u^1 \cdot \mathbf{e}_u$ , which are rotations and reflections for  $\mathbb{R}^n$ .  $\mathcal{U}_u$  induces transformations on tensor coefficients:  $\mathbf{T}_{\vec{u}} \mapsto (\mathcal{U}_{u_1} \otimes \mathcal{U}_{u_2} \otimes \dots \otimes \mathcal{U}_{u_N}) \mathbf{T}_{\vec{u}}$ , and an intuitive example

<sup>1</sup>We additionally allow for  $\mathbf{0} \in \{\mathbf{e}_{u;v_u}\}$  to represent features in  $\mathbf{T}$  that transform as scalars.

<sup>2</sup>For example, if there are  $d = 5$  points defined in the 3-dimensional Euclidean space  $\mathbb{R}^3$  and each point is associated with a standard basis  $(x, y, z)$ , then for the example of  $N=4$ , there are  $5^4$  sub-tensors and each sub-tensor  $\mathbf{T}_{(u_1, u_2, u_3, u_4)}$  contains  $3^4 = 81$  elements with indices spanning from  $xxxx$  to  $zzzz$ . In total,  $\mathbf{T}$  contains  $(5 \times 3)^4$  coefficients. The coefficients of  $\mathbf{T}$  are in general complex-valued as formally discussed in Definition 1, but are real-valued for the special case introduced in Definition 1.

for infinitesimal basis rotations in  $N = 2, n = 2$  is shown in Figure 2; (b) Tensor index permutations:  $(\vec{u}, \vec{v}) \mapsto \sigma(\vec{u}, \vec{v})$ ; (c) Global translations:  $\mathbf{x} \mapsto \mathbf{x} + \mathbf{x}_0$ . For conciseness, we borrow the term  $G$ -equivariance to say  $\hat{\mathcal{F}}_\theta$  is equivariant to all the symmetry transformations listed above.

To reiterate, **our goal** is to propose neural networks  $\hat{\mathcal{F}}_\theta$  that are not only  $G$ -equivariant, but also scalable for general values of  $N$  and  $n$ , and efficient for implementation and training in practice.

## 4 Unitary $N$ -body tensor equivariant neural network (UNiTE)

We propose our Unitary  $N$ -body Tensor Equivariant (UNiTE) neural network architecture (Figure 3). Given an input  $N$ -body tensor, UNiTE first performs an efficient tensor order reduction on diagonal sub-tensors to generate a set of representations  $\mathbf{h}^{t=0}$ . Then it updates the representations with  $t_1$  stacks of convolution, message-passing, and point-wise interaction blocks, followed by  $t_2$  stacks of point-wise self interaction blocks. Finally, a pooling operation is applied to the final representations  $\mathbf{h}^{t=t_f}$  at  $t_f = t_1 + t_2$  to readout the predictions.

### 4.1 Convolutions and message passing on $\mathbf{T}$

**Convolution in sub-tensors.** In an update step  $\mathbf{h}^t \mapsto \mathbf{h}^{t+1}$ , sub-tensors of  $\mathbf{T}$  are contracted with products of the order-1 (i.e. vectors) representations  $\mathbf{h}^t$ :

$$(\mathbf{m}_{\vec{u}}^t)_{v_1}^i = \sum_{v_2, \dots, v_N} T_{\vec{u}}(v_1, v_2, \dots, v_N) \prod_{j=2}^N (\rho_{u_j}(\mathbf{h}_{u_j}^t))_{v_j}^i \quad (3)$$

which can be viewed as a  $(N - 1)$ -dimensional convolution operation between each sub-tensor  $\mathbf{T}_{\vec{u}}$  (as convolution kernels) and the signal  $\prod_{j=2}^N \mathbf{h}_{u_j}^t$  in the  $i$ -th convolution channel. This  $(N - 1)$ -dimensional convolution gives an order-1 tensor output  $\mathbf{m}_{\vec{u}}^t$  for each sub-tensor index  $\vec{u}$ .  $\rho_u$  is called a *matching layer* at index  $u$ , which will be defined later.

**Message-passing on convolution outputs.**  $\mathbf{m}_{\vec{u}}^t$  are then aggregated into each index  $u$  by summing over the indices  $u_2, u_3, \dots, u_N$ , analogous to a ‘message-passing’ between nodes and edges in common realizations of graph neural networks [15]. We define the following equivariant message passing scheme on the (hyper-)graph defined by the set of indices  $\vec{u}$  where  $\mathbf{T}_{\vec{u}}$  is non-zero:

$$\tilde{\mathbf{m}}_{u_1}^t = \sum_{u_2, u_3, \dots, u_N} \bigoplus_i (\mathbf{m}_{\vec{u}}^t)^i \cdot \alpha_{\vec{u}}^t \quad (4)$$

$$\mathbf{h}_{u_1}^{t+1} = \phi(\mathbf{h}_{u_1}^t, \rho_{u_1}^\dagger(\tilde{\mathbf{m}}_{u_1}^t)) \quad (5)$$

where  $\alpha_{\vec{u}}^{t,j}$  are reference-frame-invariant, scalar-valued weights for improving the network capacity, and their practical parameterizations are discussed in Appendix C. In Equation 5, the aggregated equivariant messages  $\tilde{\mathbf{m}}_{u_1}^t$  are interacted with  $\mathbf{h}_{u_1}^t$  through an point-wise interaction block  $\phi(\cdot, \cdot)$  to complete the update  $\mathbf{h}_{u_1}^t \mapsto \mathbf{h}_{u_1}^{t+1}$ , which we elaborate in Section 4.3. Equations 3-5 form the backbone of UNiTE, which can be shown to satisfy  $G$ -equivariance (see Appendix A for proofs).

### 4.2 Embedding through diagonal sub-tensor reduction

Here we take a step backward and discuss the construction of initial order-1 representations,  $\mathbf{h}^{t=0}$ . We note that in general those order-1 embeddings can be *uniquely* extracted from the diagonal sub-tensors of the  $N$ -body tensor  $\mathbf{T}$  based on group representation theory. We use the short-hand notation  $\mathbf{T}_u$  to denote the  $u$ -th diagonal sub-tensors of  $\mathbf{T}$ , i.e.  $\{\mathbf{T}_u\} := \{\mathbf{T}_{\vec{u}}; u_1 = u_2 = \dots = u_N = u\}$ .

**Theorem 1 (Diagonal sub-tensors of an  $N$ -body tensor are reducible)** *(Informal)  $\mathbf{T}_u$  can be uniquely expressed as a linear combination of order-1 tensors (i.e. vectors). Such a linear combination coefficients do not depend on  $\mathbf{T}$ . Those order-1 tensors transform under the irreducible representations of the group  $O(n)$  when rotating or reflecting the reference frames.*

The above theorem is a consequence of group representation properties of  $O(n)$  and realizing that  $\mathbf{T}_u$  has a symmetric tensor decomposition which allows for identifying a special case of the Schur–Weyl duality. See Appendix A for a formal statement and proof. Based upon Theorem 1, we can obtain a practically useful result for generating the desired order-1 embeddings  $\mathbf{h}_u^{t=0}$  from  $\mathbf{T}_u$ :

**Lemma 1** Let  $(\pi_l)_m$  denote the  $m$ -th basis component for the  $l$ -th irreducible representation of  $O(n)$ . For each allowed  $l, m$ , there exist  $K_{lm} \times n^N$   $\mathbf{T}$ -independent scalar coefficients  $Q_{klm}^{\vec{v}}$  parameterizing a linear transformation  $\psi$  that performs  $\mathbf{T}_{\vec{u}} \mapsto \mathbf{h}_u$ , if  $u_1 = u_2 = \dots = u_N = u$ :

$$(\psi(\mathbf{T}_u))_{klm} := \sum_{\vec{v}} T_u(v_1, v_2, \dots, v_N) Q_{klm}^{\vec{v}} \quad \text{for } k \in \{1, 2, \dots, K_{lm}\} \quad (6)$$

such that the linear map  $\psi$  is injective,  $\sum_{l,m} K_{lm} \leq n^N$ , and for each  $g_u \in O(n)$ :

$$\psi(g_u(\mathbf{T}_u))_{kl} = \pi_l(g_u) \cdot (\psi(\mathbf{T}_u))_{kl} \quad (7)$$

**Wigner-Eckart layer  $\psi$ .** Lemma 1 implies that we can use a fixed set of at most  $n^{2N}$  coefficients  $\mathbf{Q}$  to uniquely map the diagonal sub-tensors of  $\mathbf{T}$  to order-1  $G$ -equivariant embeddings  $\mathbf{h}_u^{t=0} := \psi(\mathbf{T}_u)$ , without solving tensor factorization on  $\mathbf{T}_u$ .  $\mathbf{Q}$  can be shown to further decompose into products of  $O(n)$  Clebsch-Gordan coefficients which can simplify the contraction (6), and in practice  $\mathbf{Q}$  can be numerically tabulated using integrals of radial functions and spherical harmonics (see Appendix A and B.3). Lemma 1 can be regarded as a generalization of the Wigner-Eckart theorem originally defined for  $(N = 2, n = 3)$ , therefore we also refer to  $\psi$  defined in (6) as a *Wigner-Eckart layer*.

### 4.3 Interacting and normalizing representations with equivariance

**Equivariant Normalization (EvNorm).** We propose a normalization scheme on order-1 tensors to improve generalization while preserving  $G$ -equivariance. Given an order-1 tensor  $\mathbf{x}$ , we define  $\text{EvNorm} : \mathbf{x} \mapsto (\bar{\mathbf{x}}, \hat{\mathbf{x}})$  where  $\bar{\mathbf{x}}$  and  $\hat{\mathbf{x}}$  are given by

$$\bar{x}_{kl} := \frac{\|\mathbf{x}_{kl}\| - \mu_{kl}^x}{\sigma_{kl}^x} \quad \text{and} \quad \hat{x}_{klm} := \frac{x_{klm}}{\|\mathbf{x}_{kl}\| + 1/\beta_{kl} + \epsilon} \quad (8)$$

where  $k$  index a feature channel,  $\mu_{kl}^x$  and  $\sigma_{kl}^x$  are mean and variance estimates of the invariant content  $\|\mathbf{x}\|$ ; they can be obtained from either batch or layer statistics as in normalization schemes developed for scalar neural networks [28, 29];  $\beta_{kl}$  are positive, learnable scalars controlling the fraction of vector scale information from  $\mathbf{x}$  to be retained in  $\hat{\mathbf{x}}$ , and  $\epsilon$  is a numerical stability factor. The proposed EvNorm operation (8) decouples the order-1 tensor  $\mathbf{x}$  to the normalized scalar-valued tensor  $\bar{\mathbf{x}}$  suitable for being transformed by an MLP, and a ‘pure-direction’ tensor  $\hat{\mathbf{x}}$  that can be later multiplied to the MLP-transformed normalized invariant content to finish updating  $\mathbf{x}$ . Note that in (8), zero is always a fixed point of the map  $\mathbf{x} \mapsto \hat{\mathbf{x}}$  and the vector directions information  $\mathbf{x}$  is always preserved.

**Point-wise interaction block  $\phi$ .** We propose a *point-wise interaction block* ( $\phi$  in (5)) as a modular component to construct  $\hat{\mathcal{F}}_\theta$ , which equivariantly update  $\mathbf{h}_u^{t+1} = \phi(\mathbf{h}_u^t, \mathbf{g}_u)$  by coupling another order-1 (i.e. vector) tensor  $\mathbf{g}_u$  (e.g.  $\tilde{\mathbf{m}}_u^t$  in (5), or  $\mathbf{h}_u^t$  itself) with  $\mathbf{h}_u^t$ , and performing normalizations:

$$\mathbf{f}_u^t = \text{MLP}_1(\bar{\mathbf{h}}_u^t) \odot \hat{\mathbf{h}}_u^t \quad \text{where} \quad (\bar{\mathbf{h}}_u^t, \hat{\mathbf{h}}_u^t) = \text{EvNorm}(\mathbf{h}_u^t) \quad (9)$$

$$(\mathbf{q}_u)_{klm} = (\mathbf{g}_u)_{klm} + \sum_{l_1, l_2} \sum_{m_1, m_2} (\mathbf{f}_u^t)_{kl_1 m_1} (\mathbf{g}_u)_{kl_2 m_2} C_{l_1 m_1; l_2 m_2}^{lm} \quad (10)$$

$$\mathbf{h}_u^{t+1} = \mathbf{h}_u^t + \text{MLP}_2(\bar{\mathbf{q}}_u) \odot \hat{\mathbf{q}}_u \quad \text{where} \quad (\bar{\mathbf{q}}_u, \hat{\mathbf{q}}_u) = \text{EvNorm}(\mathbf{q}_u) \quad (11)$$

where  $C_{l_1 m_1; l_2 m_2}^{lm}$  are Clebsch-Gordan coefficients known for relating vectors to their tensor products, and  $\text{MLP}_1$  and  $\text{MLP}_2$  denote multi-layer perceptrons. See Appendix A for the proof on  $G$ -equivariance.

**Symmetry-informed pooling.** Once the representations  $\mathbf{h}_u^t$  are updated to the last step  $\mathbf{h}_u^{t_f}$ , a pooling operation  $\{\mathbf{h}_u^{t_f}\} \mapsto \mathbf{y}_\theta$  can be employed to readout the target prediction. Due to equivariance, we can flexibly address the the symmetry prior of the learning task by designing pooling schemes without modifying the model architecture. For quantum-chemistry tasks, we define a class of pooling operations detailed in Appendix B.4; for example, a molecule’s dipole vector can be predicted as  $\vec{\mu} = \sum_u (\vec{r}_u \cdot q_u + \vec{\mu}_u)$  where  $\vec{r}_u$  is the atom  $u$ ’s position, and atomic charges  $q_u$  and atomic dipoles  $\vec{\mu}_u$  can be respectively predicted using scalar ( $l = 0$ ) and vector ( $l = 1$ ) components of  $\mathbf{h}_u^{t_f}$ .

**Matching layer**  $\rho_u$ . One subtlety that must be addressed for the convolution-message-passing layers (3-5) is that the basis  $\mathbf{e}_u$  for the local reference frame at point  $u$  may differ from the underlying basis for the vector representations  $\mathbf{h}_u^t$ . However, we can construct matching layers  $\rho_u$  and  $\rho_u^\dagger$  to connect the representations defined on the two sets of basis:

$$(\rho_u(\mathbf{h}_u^t))_v^i = \sum_{l,m} \mathbf{W}_l^i \cdot (\mathbf{h}_u^t)_{lm} \cdot \langle \mathbf{e}_{u,v}, (\boldsymbol{\pi}_l)_m \rangle \quad (12)$$

$$(\rho_u^\dagger(\tilde{\mathbf{m}}_u^t))_{lm} = \sum_v \mathbf{W}_l^\dagger \cdot (\tilde{\mathbf{m}}_u^t)_v \cdot \langle (\boldsymbol{\pi}_l)_m, \mathbf{e}_{u,v} \rangle \quad (13)$$

where  $\mathbf{W}_l, \mathbf{W}_l^\dagger$  are learnable linear functions, and a careful treatment for the inner product  $\langle \mathbf{e}_u, \boldsymbol{\pi} \rangle$  will be discussed in Appendix C. For a simple example that  $\mathbf{e}_u$  is the standard basis of  $\mathbb{R}^3$  and there is only one convolution channel  $i$ ,  $\rho_u^\dagger$  is (up to a constant) given by  $(\rho_u^\dagger(\mathbf{v}))_{l=1,p=1,m} = Y_{l=1,m}(\mathbf{v})$  and  $(\rho_u^\dagger(\mathbf{v}))_{l \neq 1,p,m} \equiv 0$ , where  $\mathbf{v} \in \mathbb{R}^3$  and  $Y_{lm}$  is the spherical harmonic of degree  $l$  and order  $m$ .

**Time complexity.** The asymptotic time complexity of UNiTE is  $\mathcal{O}(BNI)$ , where  $B$  is the number of indices  $(\vec{u}, \vec{v})$  such that  $T_{\vec{u},\vec{v}} \neq 0$  (i.e., the number of non-zero elements in  $\mathbf{T}$ ), and  $I$  denotes the number of convolution channels in a convolution block (3). This implies UNiTE scales as  $\mathcal{O}(N(nd)^N)$  if the  $N$ -body tensor  $\mathbf{T}$  is dense, but can achieve a lower time complexity if  $\mathbf{T}$  is sparse.

*Proof. (Informal)* In each convolution block (3) the summand  $T_{\vec{u},\vec{v}} \cdot \prod_{j=2}^N (\rho_{u_j}(\mathbf{h}_{u_j}^t))_{v_j}^i \neq 0$  only if the tensor coefficient  $T_{\vec{u},\vec{v}} \neq 0$ ; therefore (3) can be exactly evaluated using  $((N-1)BI)$  arithmetic operations. It can be shown that in each message passing block (4) the number of arithmetic operations scales as  $\mathcal{O}(B'I)$  where  $B'$  is the number of indices  $\vec{u}$  such that  $\mathbf{m}_{\vec{u}}^t \neq 0$ , and  $B' \leq B$ . It can be shown that the embedding block  $\phi$  and the point-wise interaction block  $\psi$  has  $\mathcal{O}(d)$  time complexities and do not contribute to the asymptotic time complexity.

Several more technical aspects, including the case of multiple input channels and efficient implementations are discussed in Appendix C.

## 5 Experimental results

**Problem statement.** Quantum chemistry studies interactions among atoms and electrons in a molecular system. We aim to learn quantum chemistry properties through utilizing 2-body tensor representations for molecules originated from physical approximations on such electron-atom interactions, in this work using a semi-empirical quantum mechanics model. A scientific background and the semi-empirical tight-binding quantum chemistry approach employed to generate the tensor-based molecular representation are provided in Appendix B.1-B.2. We note that compared to methods that were developed for solely utilizing molecular geometry inputs, constructing this physics-based molecular representation incurs a moderate computational overhead; model inference time breakdowns and discussions are provided in Appendix E.2. All the ground-truth labels of the benchmarks were generated based on a conventional numerical method, i.e. Density Function Theory (DFT).

We first explore UNiTE’s performance on learning quantum-chemical properties including single-point energy, forces, dipole moment, electron density, molecular orbital energies and thermal properties on several open-source machine learning datasets. Then, using a UNiTE model trained only on energies, we perform zero-shot generalization to a variety of quantum chemical benchmarks, with comparison to physics-based and ML models. See Appendix D for hyperparameter and training details.

### 5.1 QM9

The QM9 dataset [30] contains 134k small organic molecules with up to 9 heavy (CNOF) atoms in their equilibrium geometries, with scalar-valued chemical properties computed by DFT. Due to its simple chemical composition and multiple tasks, QM9 is widely used to benchmark deep learning methods [19–22, 26, 31]. Following previous works, we use 110000 random samples as the training set and another 10831 samples as the test set. As shown in Table 1, we observe state-of-the-art performance on all 12 targets with a 150% average decrease of MAE relative to the second best

Table 1: Prediction MAEs on QM9 for models trained on 110k samples. The best results on each task are marked in bold and the second-bests are indicated by underline. The results on first 8 tasks are obtained with a preconditioning strategy based on the physical approximation used to construct the molecular representation (see Appendix B.4). UNiTE achieves state-of-the-art on all 12 targets, outperforming the second-best (SphereNet) by 150% on average.

Target	Unit	SchNet	PhysNet	Cormorant	DimeNet++	PaiNN	SphereNet	UNiTE
$\mu$	mD	33	53	38	29.7	<u>12</u>	26.9	<b>6.3</b>
$\epsilon_{\text{HOMO}}$	meV	41	34	32.9	24.6	27.6	<u>23.6</u>	<b>9.9</b>
$\epsilon_{\text{LUMO}}$	meV	34	24.7	38	19.5	20.4	<u>18.9</u>	<b>12.7</b>
$\Delta\epsilon$	meV	63	42.5	38	32.6	45.7	<u>32.3</u>	<b>17.3</b>
$U_0$	meV	14	8.2	22	6.3	<u>5.9</u>	6.3	<b>3.5</b>
$U$	meV	19	8.3	21	6.3	<u>5.8</u>	7.3	<b>3.5</b>
$H$	meV	14	8.4	21	6.5	<u>6.0</u>	6.4	<b>3.5</b>
$G$	meV	14	9.4	20	7.6	<u>7.4</u>	8.0	<b>5.2</b>
$\alpha$	$a_0^3$	0.235	0.062	0.085	<u>0.044</u>	0.045	0.047	<b>0.036</b>
$\langle R^2 \rangle$	$a_0^2$	0.073	0.765	0.961	0.331	<u>0.066</u>	0.292	<b>0.030</b>
ZPVE	meV	1.7	1.4	2.0	1.2	1.3	<b>1.1</b>	<b>1.1</b>
$c_v$	$\frac{\text{cal}}{\text{molK}}$	0.033	0.028	0.026	0.023	0.024	<b>0.022</b>	<b>0.022</b>
std. MAE	%	1.76	1.37	1.44	0.98	1.01	0.94	<b>0.47</b>
log. MAE	-	-5.2	-5.4	-5.0	-5.7	-5.8	-5.7	<b>-6.4</b>

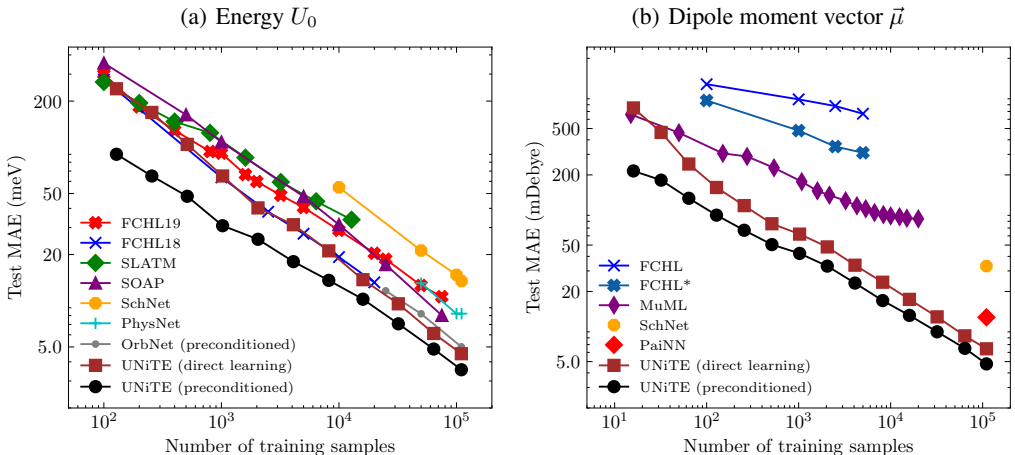


Figure 4: Comparing UNiTE to task-specific models and deep learning methods for (a) energy  $U_0$  and (b) dipole moment vector  $\vec{\mu}$  on QM9 at different training data sizes. Results obtained with the preconditioning strategy (black) and obtained with direct learning (dark red) are both included.

model. Especially, UNiTE achieves qualitative improvements on dipole norm  $\mu$ , electronic spatial extent  $\langle R^2 \rangle$ , HOMO/LUMO energies and gap  $\epsilon_{\text{HOMO}}$ ,  $\epsilon_{\text{LUMO}}$ ,  $\Delta\epsilon$ , which are deeply rooted in the electronic structure in their formulations. We also perform experiments on two representative targets, energy  $U_0$  and dipole vector  $\vec{\mu}$ , for which a plethora of task-specific ML models has previously been developed [32–37]; as shown in Figure 4, UNiTE outperforms not only deep learning methods but also kernel methods with expert-engineered features across all sizes of training data. “Direct learning” in Figure 4 corresponds to models trained from randomly-initialized parameters, and “preconditioned” corresponds to models with outputs initialized using known physical approximations, as explained in Appendix B.4.1-B.4.2. See Appendix F.2 for reference calculation details of  $\vec{\mu}$ . Uncertainty estimations on the reported prediction error statistics are provided in Appendix E.4.

Table 2: Electron charge density learning statistics. UNiTE outperforms baselines by 52% on BFDb-SSI and 75% on QM9 in  $\epsilon_\rho$  with significant training or inference efficiency advantages.

Dataset	Training samples	Mean test error $\epsilon_\rho$ (%)		
		SA-GPR	DeepDFT	UNiTE (Ours)
BFDb-SSI [41]	2000	0.29	-	<b>0.191±0.003</b>
QM9 [30]	123835	-	0.36	<b>0.206±0.001</b>

Table 3: Benchmarking UNiTE against representative semi-empirical quantum mechanics (SEQM), machine learning (ML), and density functional theory (DFT) methods on down-stream tasks.

Task	Benchmark	Metric	SEQM	ML	DFT	(Ours)
			GFN2-xTB	ANI-2x	B97-3c	UNiTE
Speed <sup>3</sup>	[44]	Relative time-to-solution↓	~5	~4	~200	~1
Data efficiency	-	Training dataset size ↓	-	8.9M	-	236K
Drug chemistry coverage	[44]	Sample coverage rate ↑	100%	81%	100%	100%
General chemistry coverage	[45]	Subset coverage rate ↑	100%	36%	100%	67%
Conformer ordering	[44]	$R^2$ [DLPNO] ↑	0.63±0.04	0.63±0.06	<b>0.90±0.01</b>	<b>0.89±0.02</b>
Torsion profiles	[46]	MAE (kcal/mol) ↓	0.73±0.01	0.90±0.01	0.29±0.00	<b>0.17±0.00</b>
Reaction energies	[45]	WTMAD-2 ↓	36.1±3.8	19.2±10.1	<b>14.6±1.6</b>	<b>14.6±4.3</b>
Intra-molecular interactions	[45]	WTMAD-2 ↓	25.1±2.4	29.6±5.8	<b>8.6±0.9</b>	10.3±1.7
Geometry optimizations	[47] [48]	RMSD (Å) ↓	0.21±0.08 0.60±0.06	- -	<b>0.06±0.01</b> 0.51±0.07	<b>0.06±0.01</b> <b>0.18±0.02</b>

## 5.2 MD17

The MD17 dataset [38] contains energy and force labels from molecular dynamics trajectories of small organic molecules, and is used to benchmark ML methods for modelling a single instance of a molecular potential energy surface. Recently the revised-MD17 (rMD17) dataset[39] was reported with improved label fidelity. For both the MD17 and the rMD17 dataset, We train UNiTE simultaneously on energies and forces of 1000 geometries of each molecule and test on another 1000 geometries of the same molecule, using reported dataset splits and revised labels (see Appendix D for details). As shown in Table E1 and Table E2, UNiTE with direct learning achieves competitive or better accuracies when compared to kernel methods [39, 40] and graph neural networks [20, 24, 25], and additional performance gains are observed when using preconditioning.

## 5.3 Electron density

We next focus on the more challenging task of predicting the electron density of molecules  $\rho(\vec{r}) : \mathbb{R}^3 \rightarrow \mathbb{R}$  which plays an essential role in both the theoretical formulation and practical construction of DFT, and in the interpretation of molecular electronic structure more broadly. Equivariance enables UNiTE to efficiently learn  $\rho(\vec{r})$  in a compact spherical expansion basis (see Appendix B.4.6). As shown in Table 2, compared to two baselines [42, 43] developed for learning  $\rho(\vec{r})$ , UNiTE achieves 50-75% reduction in mean  $L^1$  density error  $\epsilon_\rho := \frac{\int |\rho(\vec{r}) - \rho_\theta(\vec{r})| d\vec{r}}{\int |\rho(\vec{r})| d\vec{r}}$  where  $\rho_\theta(\vec{r})$  denotes the model-predicted electron density. We use a 3D cubic grid of voxel spacing (0.2, 0.2, 0.2) Bohr with cutoff at  $\rho(\vec{r}) = 10^{-5}$  (Bohr<sup>-3</sup>) to compute  $\epsilon_\rho$  for each molecule. Remarkably, UNiTE is also more efficient at training compared to SA-GPR [42] which has a cubic training time complexity, and at inference compared to DeepDFT [43] which requires evaluating part of the neural network at each grid point  $\vec{r}$ .

<sup>3</sup>All based on CPU timings. While neural networks are better parallelized on GPUs, no GPU-based implementations are available for GFN2-xTB and B97-3c and we report timings with the same hardware setup.

## 5.4 Down stream chemistry tasks

To evaluate UNiTE’s performance as a black-box quantum chemistry method, we train a UNiTE model on the DFT energies of 236k samples with broad chemical space coverage, non-equilibrium geometries, and include charged systems (see Appendix F.1). Without any model fine-tuning, we directly apply it to down-stream tasks commonly used to benchmark quantum-chemistry simulation methods (detailed in Appendix F.3). In this zero-shot setting, our pretrained model achieves accuracy similar or better than a popular DFT method [49] while being around 200x faster on CPUs (>1000x if running ours on GPUs), and is significantly better than representative semi-empirical quantum mechanics methods [50] or machine learning methods [51] which offer comparable speeds.

## 6 Discussion and conclusions

We propose UNiTE, a neural network framework for learning general  $N$ -body tensors. It shows superior performance when applied to quantum chemistry, achieving up to three orders of magnitude speedup compared to DFT on down stream chemical tasks. A limitation of our approach is the model cannot be applied to several edge cases such as all diagonal sub-tensors are zeros, therefore is not universal; however we expect such examples to be rare in physical sciences. A natural future direction is to extend the formalism to general asymmetric order- $N$  tensors through representation-theoretic techniques. While the current implementation to quantum-chemistry tasks requires solving a tight-binding model beforehand which has a cubic asymptotic time complexity with respect to the number of atoms in the molecular system, a future direction is to formulate sparse or separate-length-scale molecular representations to make the approach scalable to systems with millions of atoms. Given its demonstrated performance on practical tasks, we anticipate UNiTE to be useful in scientific applications in chemistry, quantum physics and other domains.

### Broader Impacts

Our contribution is a neural network framework with primary focus on tensor-based problems in physical sciences. Data used in this study do not contain human-related or offensive content. Although we do not foresee any direct negative societal impacts associated with human-related objects, we note that training the model may produce carbon emissions that should be taken into consideration for large-scale application scenarios. However, we also anticipate our approach to reduce carbon footprint in long terms by replacing more compute-intensive solvers. We expect our approach to be practically beneficial to the society when applied to tasks such as drug discovery and the study of elementary particles.

## A Problem setup, model architecture and proofs

We formally introduce the problem of interest, restate the definitions of the building blocks of UNiTE (Section 4) using those formal notations, and prove the theoretical results claimed in this work.

### A.1 $N$ -body tensors

**Definition A1** Let  $G_1, G_2, \dots, G_d$  denote unitary groups where  $G_u \subset U(n)$  are closed subgroups of  $U(n)$  for each  $u \in \{1, 2, \dots, d\}$ . We denote  $G := G_1 \times G_2 \times \dots \times G_d$ . Let  $(\pi_L, \mathbb{V}^L)$  denote a irreducible unitary representation of  $U(n)$  labelled by  $L$ . For each  $u \in \{0, 1, \dots, d\}$ , we assume there is a finite-dimensional Banach space  $V_u \simeq \bigoplus_L (\mathbb{V}^L)^{\oplus K_L}$  where  $K_L \in \mathbb{N}$  is the multiplicity of  $\mathbb{V}^L$  (e.g. the number of feature channels associated with representation index  $L$ ), with basis  $\{\pi_{L,M}\}_u$  such that  $\text{span}(\{\pi_{L,M,u}; k, L, M\}) = V_u$  for each  $u \in \{1, 2, \dots, d\}$  and  $k \in \{1, 2, \dots, K_L\}$ , and  $\text{span}(\{\pi_{L,M,u}; M\}) \simeq \mathbb{V}^L$  for each  $u, L$ . We denote  $\mathcal{V} := \bigoplus_u V_u$ , and index notation  $v := (k, L, M)$ . For a tensor  $\hat{\mathbf{T}} \in \mathcal{V}^{\otimes N}$ , we call the coefficients  $\mathbf{T}$  of  $\hat{\mathbf{T}}$  in the  $N$ -th direct products of basis  $\{\pi_{L,M,u}; L, M, u\}$  an  $N$ -body tensor, if  $\hat{\mathbf{T}} = \sigma(\hat{\mathbf{T}})$  for any permutation  $\sigma \in \text{Sym}(N)$  (i.e. permutation invariant). Note that the vector spaces  $V_u$  do not need to be embed in the same space  $\mathbb{R}^n$  as in the special case from Definition 1, but can be originated from general ‘parameterizations’  $u \mapsto V_u$ , e.g. from a collection of coordinate charts on a manifold.

**Corollary A1** If  $V_u = \mathbb{C}^n$ ,  $G_u = U(n)$  and  $\pi_{L,M,u} = \mathbf{e}_M$  where  $\{\mathbf{e}_M\}$  is a standard basis of  $\mathbb{C}^n$ , then  $\mathbf{T}$  is an  $N$ -body tensor if  $\hat{\mathbf{T}}$  is permutation invariant.

*Proof.* Note that when  $V_u = \mathbb{C}^n$ ,  $\pi : G_u \rightarrow U(\mathbb{C}^n)$  is a fundamental representation of  $U(n)$ . Since the fundamental representations of a Lie group are irreducible, it follows that  $\{\mathbf{e}_M\}$  is a basis of a irreducible representation of  $U(n)$ , and  $\mathbf{T}$  is an  $N$ -body tensor.

Similarly, when  $V_u = \mathbb{R}^n$  and  $G_u = O(n) \subset U(n)$ ,  $\mathbf{T}$  is an  $N$ -body tensor if  $\hat{\mathbf{T}}$  is permutation invariant. Then we can recover the special case based on point clouds in  $\mathbb{R}^n$  in Definition 1.

Procedures for constructing complete bases for irreducible representations of  $U(n)$  with explicit forms are well established [52]. A special case is  $G_u = \text{SO}(3)$ , for which a common construction of a complete set of  $\{\pi_{L,M}\}_u$  is using the spherical harmonics  $\pi_{L,M,u} := Y_{lm}$ ; this is an example that polynomials  $Y_{lm}$  can be constructed as a basis of square-integrable functions on the 2-sphere  $L^2(S^2)$  and consequently as a basis of the irreducible representations  $(\pi_L, \mathbb{V}^L)$  for all  $L$  [53].

### A.2 Decomposition of $\mathbf{T}_u$ and the Wigner-Eckart layer

We consider the algebraic structure of the diagonal sub-tensors  $\mathbf{T}_u$ , which can be understood from tensor products of irreducible representations.

First we note that for a sub-tensor  $\mathbf{T}_{\vec{u}} \in V_{u_1} \otimes V_{u_2} \otimes \dots \otimes V_{u_N}$ , the action of  $g \in G$  is given by

$$g \cdot \mathbf{T}_{\vec{u}} = (\pi(g_{u_1}) \otimes \pi(g_{u_2}) \otimes \dots \otimes \pi(g_{u_N})) \mathbf{T}_{\vec{u}} \quad (\text{A1})$$

for diagonal sub-tensors  $\mathbf{T}_u$ , this reduces to the action of a diagonal sub-group

$$g \cdot \mathbf{T}_u = (\pi(g_u) \otimes \pi(g_u) \otimes \dots \otimes \pi(g_u)) \mathbf{T}_u \quad (\text{A2})$$

which forms a representation of  $G_u \in U(n)$  on  $V_u^{\otimes N}$ . According to the isomorphism  $V_u \simeq \bigoplus_L (\mathbb{V}^L)^{\oplus K_L}$  in Definition A1 we have  $\pi(g_u) \cdot \mathbf{v} = \bigoplus_L U_{g_u}^L \cdot \mathbf{v}_L$  for  $\mathbf{v} \in V_u$  where  $\mathbf{v}_L \in \mathbb{V}^L$ , more explicitly

$$g \cdot \mathbf{T}_u(\vec{k}, \vec{L}) = (U_{g_u}^{L_1} \otimes U_{g_u}^{L_2} \otimes \dots \otimes U_{g_u}^{L_N}) \mathbf{T}_u(\vec{k}, \vec{L}) \quad (\text{A3})$$

where we define the shorthand notation  $\mathbf{T}_u(\vec{k}, \vec{L}) := \mathbf{T}_u((k_1, L_1), (k_2, L_2), \dots, (k_N, L_N))$  and  $U_{g_u}^L$  denotes the unitary matrix representation of  $g_u \in U(n)$  on  $\mathbb{V}^L$  expressed in the basis  $\{\pi_{L,M,u}; M\}$ , on the vector space  $\mathbb{V}^L$  for the irreducible representation labelled by  $L$ . Therefore  $\mathbf{T}_u(\vec{k}, \vec{L}) \in \mathbb{V}^{L_1} \otimes \mathbb{V}^{L_2} \otimes \dots \otimes \mathbb{V}^{L_N}$  is the representation space of an  $N$ -fold tensor product representations of  $U(n)$ . We note the following theorem for the decomposition of  $\mathbf{T}_u(\vec{k}, \vec{L})$ :

**Theorem A1** (Theorem 2.1 and Corollary 2.2 of [54]) *The representation of  $U(N)$  on the direct product of  $\mathbb{V}^{L_1}, \mathbb{V}^{L_2}, \dots, \mathbb{V}^{L_N}$  decomposes into direct sum of irreducible representations:*

$$\mathbb{V}^{L_1} \otimes \mathbb{V}^{L_2} \otimes \dots \otimes \mathbb{V}^{L_N} \simeq \bigoplus_L \bigoplus_{\nu}^{\mu(L_1, L_2, \dots, L_N; L)} \mathbb{V}^{L; \nu} \quad (\text{A4})$$

and

$$\sum_L \mu(L_1, L_2, \dots, L_N; L) \dim(\mathbb{V}^L) = \prod_{u=1}^N \dim(\mathbb{V}^{L_u}) \quad (\text{A5})$$

where  $\mu(L_1, L_2, \dots, L_N; L)$  is the multiplicity of  $L$  denoting the number of replicas of  $\mathbb{V}^L$  being present in the decomposition of  $\mathbb{V}^{L_1} \otimes \mathbb{V}^{L_2} \otimes \dots \otimes \mathbb{V}^{L_N}$ .

Note that we have abstracted the labelling details for  $U(n)$  irreducible representations into the index  $L$ . See [54] for proof and details on representation labelling. We now restate Theorem 1 in terms of tensor products of irreducible representations.

**Theorem 1** *There exists an invertible linear map  $\psi : V_u^{\otimes N} \rightarrow V_u^* := \bigoplus (\mathbb{V}^L)^{\oplus \mu(L; V_u)}$  where  $\mu(L; V_u) \in \mathbb{N}$ , such that for any  $\mathbf{T}_u, L$  and  $\nu \in \{1, 2, \dots, \mu(L; V_u)\}$ ,  $\psi(g_u \cdot \mathbf{T}_u)_{\nu, L} = U_{g_u}^L \psi(\mathbf{T}_u)_{\nu, L}$  if  $\mu(L; V_u) > 0$ .*

*Proof.* First note that each block  $\mathbf{T}_u(\vec{k}, \vec{L})$  of  $\mathbf{T}_u$  is an element of  $\mathbb{V}^{L_1} \otimes \mathbb{V}^{L_2} \otimes \dots \otimes \mathbb{V}^{L_N}$  up to an isomorphism. (A5) in Theorem A1 states there is an invertible linear map  $\psi_{\vec{L}} : \mathbb{V}^{L_1} \otimes \mathbb{V}^{L_2} \otimes \dots \otimes \mathbb{V}^{L_N} \rightarrow \bigoplus_L (\mathbb{V}^L)^{\oplus \mu(L_1, L_2, \dots, L_N; L)}$ , such that  $\tau(g_u) = (\psi_{\vec{L}})^{-1} \circ \pi(g_u) \circ \psi_{\vec{L}}$  for any  $g_u \in G_u$ , where  $\tau : G_u \rightarrow U(\mathbb{V}^{L_1} \otimes \mathbb{V}^{L_2} \otimes \dots \otimes \mathbb{V}^{L_N})$  and  $\pi : G_u \rightarrow U(\bigoplus_L (\mathbb{V}^L)^{\oplus \mu(L_1, L_2, \dots, L_N; L)})$  are representations of  $G_u$ . Note that  $\pi$  is defined as a direct sum of irreducible representations of  $U(n)$ , i.e.  $\pi(g_u) \psi_{\vec{L}}(\mathbf{T}_u(\vec{k}, \vec{L})) := \bigoplus_{\nu, L} U_{g_u}^L (\psi_{\vec{L}}(\mathbf{T}_u(\vec{k}, \vec{L})))_{\nu, L}$ . Now define  $\psi(\mathbf{T}_u) := \bigoplus_L \bigoplus_{\vec{k}, \vec{L}} \psi_{\vec{L}}(\mathbf{T}_u(\vec{k}, \vec{L}))_L$  and  $\mu(L, V_u) := \sum_{\vec{k}, \vec{L}} \mu(L_1, L_2, \dots, L_N; L)$ , which directly satisfies  $\psi(g_u \cdot \mathbf{T}_u)_{\nu, L} = \psi(\tau(g_u) \mathbf{T}_u)_{\nu, L} = U_{g_u}^L \psi(\mathbf{T}_u)_{\nu, L}$  for  $\nu \in \{1, 2, \dots, \mu(L; V_u)\}$ . Since each  $\psi_{\vec{L}}$  are finite-dimensional and invertible, it follows that the finite direct sum  $\psi$  is invertible.

We also restate Lemma 1 which was originally given based on representation indices of  $O(n)$ :

**Lemma 1** *For each  $L$  where  $\mu(L; V_u) > 0$ , there exist  $n_L \times \dim(V_u)^N$   $\mathbf{T}$ -independent coefficients  $Q_{\nu, L, M}^{\vec{v}}$  parameterizing the linear transformation  $\psi$  that performs  $\mathbf{T}_{\vec{u}} \mapsto \mathbf{h}_u := \psi(\mathbf{T}_u)$ , if  $u_1 = u_2 = \dots = u_N = u$ :*

$$(\psi(\mathbf{T}_u))_{\nu, L, M} := \sum_{\vec{v}} T_u(v_1, v_2, \dots, v_N) Q_{\nu, L, M}^{\vec{v}} \quad \text{for } \nu \in \{1, 2, \dots, n_L\} \quad (\text{A6})$$

such that the linear map  $\psi$  is injective,  $\sum_L n_L \leq \dim(V_u)^N$ , and for each  $g_u \in G_u$ :

$$\psi(g_u \cdot \mathbf{T}_u)_{\nu, L} = U_{g_u}^L (\psi(\mathbf{T}_u))_{\nu, L} \quad (\text{A7})$$

*Proof.* According to Definition A1, a complete basis of  $V_u^{\otimes N}$  is given by  $\{\pi_{L_1, M_1, u} \otimes \pi_{L_2, M_2, u} \otimes \dots \otimes \pi_{L_N, M_N, u}; (\vec{k}, \vec{L}, \vec{M})\}$  and a complete basis of  $(V_u^*)_L$  is  $\{\pi_{L, M, u}; M\}$ . Note that  $V_u$  and  $(V_u^*)_L$  are both finite dimensional. Therefore an example of  $\mathbf{Q}_L$  is the  $\dim(V_u)^N \times \mu(L; V_u)$  matrix representation of the bijective map  $\psi$  in the two basis, which proves the existence.

Note that Theorem 1 does not guarantee the resulting order-1 representations  $\mathbf{h}_u := \psi(\mathbf{T}_u)$  (i.e. vectors in  $V_u^*$ ) to be invariant under permutations  $\sigma$ , as the ordering of  $\{\nu\}_L$  may change under  $\mathbf{T} \mapsto \sigma(\mathbf{T})$ . Hence, we realize that the symmetric condition on  $\mathbf{T}$  is important to achieve permutation equivariance for the decomposition  $V_u^{\otimes N} \rightarrow V_u^*$ ; we note that  $\mathbf{T}_u$  has a symmetric tensor factorization and is an element of  $\text{Sym}^N(V_u)$ , then algebraically the existence of a permutation-invariant decomposition is ensured by the Schur-Weyl duality [55] giving the fact that all representations in the decomposition of  $\text{Sym}^N(V_u)$  must commute with the symmetric group  $S_N$ . With the matrix representation  $\mathbf{Q}$  in (A6), clearly for any  $\sigma$ ,  $\psi(\sigma(\mathbf{T}_u)) = \sigma(\mathbf{T}_u) \cdot \mathbf{Q} = \mathbf{T}_u \cdot \mathbf{Q} = \psi(\mathbf{T}_u)$ . For general asymmetric  $N$ -body tensors, we expect the realization of permutation equivariance to be

more complicated and may be done through tracking the Schur functors from the Schur-Weyl duality in the decomposition of  $V_u^{\otimes N} \rightarrow V_u^*$ , and is left as a direction for future works.

Additionally, the upper bound  $\sum_L n_L \leq \dim(V_u)^N$  is in practice often not saturated and the contraction (A6) can be simplified. For example, when  $N > 2$  it suffices to perform permutation-invariant decomposition on symmetric  $\mathbf{T}_u$  using a simple recursive procedure through *Clebsch-Gordan coefficients*  $\mathbf{C}$  defined for  $N = 2$ , which has the following property:

$$\mathbf{C}_{L_1;L_2}^{\nu,L} \cdot (U_{g_u}^{L_1} \otimes U_{g_u}^{L_2}) \cdot (\mathbf{C}_{L_1;L_2}^{\nu,L})^\dagger = U_{g_u}^L \quad \text{for } \nu \in \{1, 2, \dots, \mu(L_1, L_2; L)\} \quad (\text{A8})$$

i.e.,  $\mathbf{C}$  parameterizes the isomorphism  $\psi_{\vec{L}}$  of Theorem 1 for  $N = 2$ ,  $\vec{L} = (L_1, L_2)$ . Then  $\psi$  can be constructed with the procedure  $(V_u)^{\otimes N} \mapsto V_u' \otimes (V_u)^{\otimes(N-2)} \mapsto V_u'' \otimes (V_u)^{\otimes(N-3)} \mapsto V_u^*$  without explicit order- $N + 1$  tensor contractions, where each reduction step can be parameterized using  $\mathbf{C}$ .

Procedures for computing  $\mathbf{C}$  for  $U(n)$  in general have been established [56, 57]. A specific example used for numerical experiments in this work is  $O(3) \simeq SO(3) \times \mathbb{Z}_2$ , where  $\mu(L_1, L_2; L) \leq 1$  and the basis of an irreducible representation  $\pi_{L,M}$  can be written as  $\pi_{L,M} := |l, m, p\rangle$  where  $p \in \{1, -1\}$  and  $m \in \{-l, -l+1, \dots, l-1, l\}$ .  $|l, m, p\rangle$  can be thought as a spherical harmonic  $Y_{lm}$  but may additionally flips sign under point reflections  $\mathcal{I}$  depending on the parity index  $p$ :  $\mathcal{I}|l, m, p\rangle = p \cdot (-1)^l |l, m, p\rangle$  where  $\forall \mathbf{x} \in \mathbb{R}^3, \mathcal{I}(\mathbf{x}) = -\mathbf{x}$ . Clebsch-Gordan coefficients  $\mathbf{C}$  for  $O(3)$  is given by:

$$C_{l_1 m_1; l_2 m_2}^{\nu=1, l p m} = C_{l_1 m_1; l_2 m_2}^{l m} \delta_{p_1 \cdot p_2 \cdot p}^{((-1)^{l_1+l_2+l})} \quad (\text{A9})$$

where  $C_{l_1 m_1; l_2 m_2}^{l m}$  are  $SO(3)$  Clebsch-Gordan coefficients. If  $N = 2$ , the problem reduces to using Clebsch-Gordan coefficients to decompose  $\mathbf{T}_u$  as a combination of matrix representations of *spherical tensor operators* which are linear operators transforming under irreducible representation of  $SO(3)$ , based on the the Wigner-Eckart Theorem (see [10] for formal derivations). Remarkably, a recent work [58] discussed connections of a class of neural networks to the Wigner-Eckart Theorem in the context of operators in spherical CNNs, which also provides a nice review on this topic.

Both  $V_u$  and  $V_u^*$  are defined as direct sums of the representation spaces  $\mathbb{V}^L$  of irreducible representations of  $G_u$ , but each  $L$  may be associated with a different multiplicity  $K_L$  or  $K_L^*$  (e.g. different numbers of feature channels). We also allow for the case that the definition basis  $\{\mathbf{e}_{u;v}\}$  for the  $N$ -body tensor  $\mathbf{T}$  differ from  $\{\pi_{u;L,M}\}$  by a known linear transformation  $\mathbf{D}_u$  such that  $\mathbf{e}_{u;v} := \sum_{L,M} (D_u)_v^{L,M} \pi_{u;L,M}$ , or  $(D_u)_v^{L,M} := \langle \mathbf{e}_{u;v}, \pi_{u;L,M} \rangle$  where  $\langle \cdot, \cdot \rangle$  denotes an Hermitian inner product, and we additionally define if  $K_L = 0$ ,  $\langle \mathbf{e}_{u;v}, \pi_{u;L,M} \rangle := 0$ . We then give a natural extension to Definition A1:

**Definition A2** We extend the basis in Definition A1 for  $N$ -body tensors to  $\{\mathbf{e}_{u;v}\}$  where  $\text{span}(\{\mathbf{e}_{u;v}; v\}) = V_u$ , if  $\mathbf{D}$  equivariantly maps between two equivalent representations of  $G_u$ :

$$\mathbf{D}_u \cdot \pi^2(g_u) = \pi^1(g_u) \cdot \mathbf{D}_u \quad \forall g_u \in G_u \quad (\text{A10})$$

where  $\pi^1$  and  $\pi^2$  are matrix representations of  $g_u$  on  $V_u \subset V_u^*$  in basis  $\{\mathbf{e}_{u;v}\}$  and in basis  $\{\pi_{u;L,M}\}$ . Note that  $\pi^2(g_u) \cdot \mathbf{v} = U_{g_u}^L \cdot \mathbf{v}$  for  $\mathbf{v} \in \mathbb{V}^L$ . This basis transformation is used to define the matching layers (??) to ensure equivariance when manipulating tensor coefficients defined on different basis.

### A.3 Neural network building blocks

To avoid confusions, we clarify that in all the sections below  $n$  refers to a feature channel index within a irreducible representation group labelled by  $L$ , which should not be confused with  $\dim(V_u)$ . More explicitly speaking, we note  $n \in \{1, 2, \dots, \mathcal{N}_L^h\}$  where  $\mathcal{N}_L^h$  is the number of vectors in the order-1 tensor  $\mathbf{h}_u^t$  that transforms under the  $L$ -th irreducible representation  $G_u$  (i.e. the multiplicity of  $L$  in  $\mathbf{h}_u^t$ ).  $M \in \{1, 2, \dots, \dim(\mathbb{V}^L)\}$  indicates the  $M$ -th component of a vector in the representation space of the  $L$ -th irreducible representation of  $G_u$ , corresponding to a basis vector  $\pi_{L,M,u}$ . We also denote the total number of feature channels in  $\mathbf{h}$  as  $\mathcal{N}^h := \sum_L \mathcal{N}_L^h$ .

For a simple example, if the features in the order-1 representation  $\mathbf{h}^t$  are specified by  $L \in \{0, 1\}$ ,  $\mathcal{N}_{L=0}^h = 8$ ,  $\mathcal{N}_{L=1}^h = 4$ ,  $\dim(\mathbb{V}^{L=0}) = 1$ , and  $\dim(\mathbb{V}^{L=1}) = 5$ , then  $\mathcal{N}^h = 8 + 4 = 12$  and  $\mathbf{h}_u^t$  is stored as an array with  $\sum_L \mathcal{N}_L^h \cdot \dim(\mathbb{V}^L) = (8 \times 1 + 4 \times 5) = 28$  numbers.

We reiterate that  $\vec{u} := (u_1, u_2, \dots, u_N)$  is a sub-tensor index (location of a sub-tensor in the  $N$ -body tensor  $\mathbf{T}$ ), and  $\vec{v} := (v_1, v_2, \dots, v_N)$  is an element index in a sub-tensor  $\mathbf{T}_{\vec{u}}$ .

**Convolution and message passing.** We first extend the definition of a convolution block (3) to complex numbers (as needed for  $U(n)$ ), by taking the complex conjugation on  $\mathbf{h}^t$ :

$$(\mathbf{m}_{\vec{u}}^t)_{v_1}^i = \sum_{v_2, \dots, v_N} T_{\vec{u}}(v_1, v_2, \dots, v_N) \prod_{j=2}^N (\rho_{u_j}(\mathbf{h}_{u_j}^t)^*)_{v_j}^i \quad (\text{A11})$$

The definitions for message-passing blocks (4)-(5) are unchanged, and we rewrite for completeness:

$$\tilde{\mathbf{m}}_{u_1}^t = \sum_{u_2, u_3, \dots, u_N} \bigoplus_{i, j} (\mathbf{m}_{\vec{u}}^t)^i \cdot \alpha_{\vec{u}}^{t, j} \quad (\text{A12})$$

$$\mathbf{h}_{u_1}^{t+1} = \phi(\mathbf{h}_{u_1}^t, \rho_{u_1}^\dagger(\tilde{\mathbf{m}}_{u_1}^t)) \quad (\text{A13})$$

**EvNorm.** We write the EvNorm operation (8) as  $\text{EvNorm} : \mathbf{x} \mapsto (\bar{\mathbf{x}}, \hat{\mathbf{x}})$  where

$$\bar{x}_{nL} := \frac{\|\mathbf{x}_{nL}\| - \mu_{nL}^x}{\sigma_{nL}^x} \quad \text{and} \quad \hat{x}_{nLM} := \frac{x_{nLM}}{\|\mathbf{x}_{nL}\| + 1/\beta_{nL} + \epsilon} \quad (\text{A14})$$

**Point-wise interaction  $\phi$ .** We adapt the notations and explicitly expand (9)-(11) for clarity. The operations within a point-wise interaction block  $\mathbf{h}_u^{t+1} = \phi(\mathbf{h}_u^t, \mathbf{g}_u)$  are defined as :

$$(\mathbf{f}_u^t)_{nLM} = (\text{MLP}_1(\bar{\mathbf{h}}_A^t))_{nL}(\hat{\mathbf{h}}_u^t)_{nLM} \quad \text{where} \quad (\bar{\mathbf{h}}_u^t, \hat{\mathbf{h}}_u^t) = \text{EvNorm}(\mathbf{h}_u^t) \quad (\text{A15})$$

$$(\mathbf{q}_u)_{nLM} = (\mathbf{g}_u)_{nLM} + \sum_{L_1, L_2} \sum_{M_1, M_2} (\mathbf{f}_u^t)_{nL_1 M_1} (\mathbf{g}_u)_{nL_2 M_2} C_{L_1 M_1; L_2 M_2}^{\nu(n), LM} \quad (\text{A16})$$

$$(\mathbf{h}_u^{t+1})_{nLM} = (\mathbf{h}_u^t)_{nLM} + (\text{MLP}_2(\bar{\mathbf{q}}_u))_{nL}(\hat{\mathbf{q}}_u)_{nLM} \quad \text{where} \quad (\bar{\mathbf{q}}_u, \hat{\mathbf{q}}_u) = \text{EvNorm}(\mathbf{q}_u) \quad (\text{A17})$$

where  $\nu : \mathbb{N}^+ \rightarrow \mathbb{N}^+$  assigns an output multiplicity index  $\nu$  to a group of feature channels  $n$ .

For the special example of  $O(3)$  where the output multiplicity  $\mu(L_1, L_2; L) \leq 1$  (see Theorem A1 for definitions), we can restrict  $\nu(n) \equiv 1$  for all values of  $n$ , and (A16) can be rewritten as

$$(\mathbf{q}_u)_{nlpm} = (\mathbf{g}_u)_{nlpm} + \sum_{l_1, l_2} \sum_{m_1, m_2} \sum_{p_1, p_2} (\mathbf{f}_u^t)_{nl_1 p_1 m_1} (\mathbf{g}_u)_{nl_2 p_2 m_2} C_{l_1 m_1; l_2 m_2}^{lm} \delta_{p_1 \cdot p_2 \cdot p}^{((-1)^{l_1 + l_2 + l})} \quad (\text{A18})$$

which is based on the construction of  $C_{L_1 M_1; L_2 M_2}^{\nu(n), LM}$  in (A9). The above form exactly recovers (10).

**Matching layers.** Based on Definition A2, we can rewrite the operations of a general matching layers  $\rho_u$  and  $\rho_u^\dagger$  as

$$(\rho_u(\mathbf{h}_u^t))_v^i = \sum_{L, M} (\mathbf{W}_L^i \cdot (\mathbf{h}_u^t)_{LM}) \cdot \langle \mathbf{e}_{u;v}, \boldsymbol{\pi}_{u;L, M} \rangle \quad (\text{A19})$$

$$(\rho_u^\dagger(\tilde{\mathbf{m}}_u^t))_{LM} = \sum_v \mathbf{W}_L^\dagger \cdot (\tilde{\mathbf{m}}_u^t)_v \cdot \langle \boldsymbol{\pi}_{u;L, M}, \mathbf{e}_{u;v} \rangle \quad (\text{A20})$$

where  $\mathbf{W}_L^i$  are learnable  $(1 \times \mathcal{N}_L^i)$  matrices;  $\mathbf{W}_L^\dagger$  are learnable  $(\mathcal{N}_L^i \times (\mathcal{N}^i \mathcal{N}^j))$  matrices where  $\mathcal{N}^i$  denotes the number of convolution channels (number of allowed  $i$  in (3)) and  $\mathcal{N}^j$  denotes the number of message passing weights on each  $\vec{u}$  (number of allowed  $j$  in (4)).

#### A.4 $G$ -equivariance

With main results from Theorem 1 and Lemma 1 and basic linear algebra, the equivariance of UNiTE can be straightforwardly proven.  $G$ -equivariance of the Wigner-Eckart layer  $\psi$  is stated in Lemma 1, and it suffices to prove the equivariance for other building blocks.

*Proof of  $U(n)$  equivariance for the convolution block (A11).* For any  $g \in G$ :

$$\sum_{v_2, \dots, v_N} (g \cdot T_{\vec{u}}(v_1, v_2, \dots, v_N)) \prod_{j=2}^N (\rho_{u_j}((g \cdot \mathbf{h}_{u_j}^t)^*))_{v_j}^i$$

$$\begin{aligned}
&= \sum_{v_2, \dots, v_N} \left( \left( \bigotimes_{\bar{u}} \pi^1(g_{u_j}) \cdot T_{\bar{u}} \right) (v_1, v_2, \dots, v_N) \right) \prod_{j=2}^N (\rho_{u_j} ((\pi^2(g_{u_j}) \cdot \mathbf{h}_{u_j}^t)^*))_{v_j}^i \\
&= \sum_{v_2, \dots, v_N} \left( \left( \bigotimes_{\bar{u}} \pi^1(g_{u_j}) \cdot T_{\bar{u}} \right) (v_1, v_2, \dots, v_N) \right) \prod_{j=2}^N \left( \sum_{L, M} (\mathbf{D}_{u_j})_{v_j}^{L, M} \cdot (\mathbf{W}_L^i \cdot ((\pi^2(g_{u_j}) \cdot \mathbf{h}_{u_j}^t)_{LM})^*) \right)^i \\
&= \sum_{v_2, \dots, v_N} \left( \left( \bigotimes_{\bar{u}} \pi^1(g_{u_j}) \cdot T_{\bar{u}} \right) (v_1, v_2, \dots, v_N) \right) \prod_{j=2}^N \left( \sum_{L, M} \mathbf{W}_L^i \cdot (\mathbf{D}_{u_j})_{v_j}^{L, M} \cdot (\pi^2(g_{u_j}) \cdot \mathbf{h}_{u_j}^t)_{LM} \right)^i \\
&\stackrel{(A12)}{=} \sum_{v_2, \dots, v_N} \left( \left( \bigotimes_{\bar{u}} \pi^1(g_{u_j}) \cdot T_{\bar{u}} \right) (v_1, v_2, \dots, v_N) \right) \prod_{j=2}^N \left( \sum_{L, M} (\mathbf{W}_L^i \cdot (\pi^1(g_{u_j}) \cdot \mathbf{D}_{u_j}^{L, M} \cdot \mathbf{h}_{u_j}^t)_{v_j})^* \right)^i \\
&= \sum_{v_2, \dots, v_N} \left( \left( \bigotimes_{\bar{u}} \pi^1(g_{u_j}) \cdot T_{\bar{u}} \right) (v_1, v_2, \dots, v_N) \right) \prod_{j=2}^N ((\pi^1(g_{u_j}) \cdot \rho_{u_j}(\mathbf{h}_{u_j}^t))^*)_{v_j}^i \\
&= \sum_{v_2, \dots, v_N} \left( \left( \bigotimes_{\bar{u}} \pi^1(g_{u_j}) \cdot T_{\bar{u}} \right) (v_1, v_2, \dots, v_N) \right) \prod_{j=2}^N (\pi^1(g_{u_j})^* \cdot (\rho_{u_j}(\mathbf{h}_{u_j}^t))^*)_{v_j}^i \\
&= \sum_{v_2, \dots, v_N} \sum_{v'_1, v'_2, \dots, v'_N} ((\pi^1(g_{u_j}))_{v_j, v'_j} \cdot T_{\bar{u}}(v'_1, v'_2, \dots, v'_N)) \prod_{j=2}^N \sum_{v''_j} (\pi^1(g_{u_j})^*)_{v_j, v''_j} \cdot ((\rho_{u_j}(\mathbf{h}_{u_j}^t))^*)_{v''_j}^i \\
&= \sum_{v'_1, v'_2, \dots, v'_N} (\pi^1(g_{u_1}))_{v_1, v'_1} T_{\bar{u}}(v'_1, v'_2, \dots, v'_N) \prod_{j=2}^N \sum_{v_j, v''_j} (\pi^1(g_{u_j}))_{v_j, v''_j} (\pi^1(g_{u_j})^*)_{v_j, v''_j} \cdot ((\rho_{u_j}(\mathbf{h}_{u_j}^t))^*)_{v''_j}^i \\
&= \sum_{v'_1, v'_2, \dots, v'_N} (\pi^1(g_{u_1}))_{v_1, v'_1} T_{\bar{u}}(v'_1, v'_2, \dots, v'_N) \prod_{j=2}^N \sum_{v''_j} \delta_{v''_j}^{v'_j} \cdot ((\rho_{u_j}(\mathbf{h}_{u_j}^t))^*)_{v''_j}^i \\
&= \sum_{v'_1} (\pi^1(g_{u_1}))_{v_1, v'_1} \sum_{v'_2, \dots, v'_N} T_{\bar{u}}(v'_1, v'_2, \dots, v'_N) \prod_{j=2}^N ((\rho_{u_j}(\mathbf{h}_{u_j}^t))^*)_{v'_j}^i \\
&= \sum_{v'_1} (\pi^1(g_{u_1}))_{v_1, v'_1} (\mathbf{m}_{\bar{u}}^t)_{v'_1}^i \\
&= \pi^1(g_{u_1}) \cdot (\mathbf{m}_{\bar{u}}^t)_{v'_1}^i = (g \cdot (\mathbf{m}_{\bar{u}}^t)^i)_{v_1}
\end{aligned}$$

*Proof of U(n) equivariance for the message passing block (A12)-(A13).* From the invariance condition  $g \cdot \alpha_{\bar{u}}^{t,j} = \alpha_{\bar{u}}^{t,j}$ , clearly

$$\begin{aligned}
&\sum_{u_2, u_3, \dots, u_N} \bigoplus_{i,j} (g \cdot \mathbf{m}_{\bar{u}}^t)^i \cdot \alpha_{\bar{u}}^{t,j} \\
&= \sum_{u_2, u_3, \dots, u_N} \bigoplus_{i,j} (\pi^1(g_{u_1}) \cdot (\mathbf{m}_{\bar{u}}^t)^i) \cdot \alpha_{\bar{u}}^{t,j} \\
&= \pi^1(g_{u_1}) \cdot \sum_{u_2, u_3, \dots, u_N} \bigoplus_{i,j} ((\mathbf{m}_{\bar{u}}^t)^i) \cdot \alpha_{\bar{u}}^{t,j} \\
&= \pi^1(g_{u_1}) \cdot \tilde{\mathbf{m}}_{u_1}^t = g \cdot \tilde{\mathbf{m}}_{u_1}^t
\end{aligned}$$

*Proof of U(n) equivariance for EvNorm (A14).* Note that the vector norm  $\|\mathbf{x}_{nL}\|$  is invariant to unitary transformations  $\mathbf{x}_{nL} \mapsto U_{g_u}^L \cdot \mathbf{x}_{nL}$ . Then  $\overline{(g \cdot \mathbf{x})} = \frac{\|\mathbf{x}_{nL}\| - \mu_{nL}^x}{\sigma_{nL}^x} = \bar{\mathbf{x}}$ , and  $\overline{(g \mathbf{x}_{nL})} = \frac{(\pi^2(g_u) \cdot \mathbf{x})_{nLM}}{\|\mathbf{x}_{nL}\| + 1/\beta_{nL} + \epsilon} = \pi^2(g_u) \cdot \hat{\mathbf{x}}_{nL} = g \cdot \hat{\mathbf{x}}_{nL}$ .

*Proof of U(n) equivariance for the point-wise interaction block (A15)-(A17).* Equivariances for (A15) and (A17) are direct consequences of the equivariance of EvNorm  $\overline{(g \cdot \mathbf{x})} = \bar{\mathbf{x}}$  and  $\overline{(g \mathbf{x}_{nL})} =$

$g \cdot \hat{\mathbf{x}}_{nL}$ , if  $g_u \cdot \mathbf{x}_{nL} = \pi^2(g_u) \cdot \mathbf{x}_{nL} \equiv U_{g_u}^L \cdot \mathbf{x}_{nL}$ . Then it suffices to prove  $g \cdot (\mathbf{q}_u)_{nL} = U_{g_u}^L \cdot (\mathbf{q}_u)_{nL}$ , which is ensured by (A8):

$$\begin{aligned}
& (g_u \cdot \mathbf{g}_u)_{nLM} + \sum_{L_1, L_2} \sum_{M_1, M_2} (g_u \cdot \mathbf{f}_u^t)_{nL_1 M_1} (g_u \cdot \mathbf{g}_u)_{nL_2 M_2} C_{L_1 M_1; L_2 M_2}^{\nu(n), LM} \\
&= (U_{g_u}^L \cdot \mathbf{g}_u)_{nLM} + \sum_{L_1, L_2} \sum_{M_1, M_2} (U_{g_u}^{L_1} \cdot \mathbf{f}_u^t)_{nL_1 M_1} (U_{g_u}^{L_2} \cdot \mathbf{g}_u)_{nL_2 M_2} C_{L_1 M_1; L_2 M_2}^{\nu(n), LM} \\
&= (U_{g_u}^L \cdot \mathbf{g}_u)_{nLM} + \sum_{L_1, L_2} \sum_{M_1, M_2} \sum_{M'_1, M'_2} (U_{g_u}^{L_1} \otimes U_{g_u}^{L_2})_{M_1, M'_1}^{M_2, M'_2} \cdot (\mathbf{f}_u^t)_{nL_1 M'_1} (\mathbf{g}_u)_{nL_2 M'_2} C_{L_1 M_1; L_2 M_2}^{\nu(n), LM} \\
&\stackrel{(A10)}{=} (U_{g_u}^L \cdot \mathbf{g}_u)_{nLM} + \sum_{L_1, L_2} \sum_{M'_1, M'_2} \sum_{M'} (U_{g_u}^L)_{M, M'} \cdot ((\mathbf{f}_u^t)_{nL_1 M'_1} (\mathbf{g}_u)_{nL_2 M'_2} C_{L_1 M'_1; L_2 M'_2}^{\nu(n), LM'}) \\
&= U_{g_u}^L \cdot (\mathbf{g}_u + \sum_{L_1, L_2} \sum_{M'_1, M'_2} (\mathbf{f}_u^t)_{nL_1 M'_1} (\mathbf{g}_u)_{nL_2 M'_2} C_{L_1 M'_1; L_2 M'_2}^{\nu(n), LM'})_{nLM} \\
&= U_{g_u}^L \cdot (\mathbf{q}_u)_{nLM} = \pi^2(g_u) \cdot (\mathbf{q}_u)_{nLM} = g \cdot (\mathbf{q}_u)_{nLM}
\end{aligned}$$

For permutation equivariance, it suffices to realize  $\sigma(\mathbf{T}) \equiv \mathbf{T}$  due to the symmetric condition in Definition 1 so (A11) is invariant under  $\sigma$ , the permutation invariance of  $\psi$  (see Equation A6), and the actions of  $\sigma$  on network layers in  $\phi$  defined for a single dimension  $\{(u; v)\}$  are trivial (since  $\sigma(u) \equiv u$ ). Hence the end-to-end  $G$ -equivariance of UNiTE is ensured.

## B UNiTE for Quantum Chemistry

Notations in this section are chosen to parallel the conventions in quantum chemistry, and should not be confused with several quantities with duplicated symbols from previous sections.

### B.1 Scientific background of learning tasks in Sec. 5

A molecule is formed by atomic nuclei and electrons. Although in a classical picture electrons in a molecule are represented as bound to atoms, since the founding of quantum mechanics in the 1920s, physicists realized that each electron in the molecule can in fact move in the 3D space. Their motions are dictated by the Schrödinger equation:<sup>4</sup>

$$\hat{H}\Psi(\mathbf{r}_e) = E(\mathbf{R})\Psi(\mathbf{r}_e) \quad (\text{B1})$$

where  $\mathbf{r}_e$  denotes the positions of electrons, and  $\mathbf{R}$  denotes the positions of atomic nuclei. Each electron is moving in the 3-dimensional space, so for a molecule with  $N$  electrons,  $\mathbf{r}_e$  can be thought as a  $3N$  dimensional vector in  $\mathbb{R}^{3N}$ .  $\Psi : \mathbb{R}^{3N} \rightarrow \mathbb{R}$  is called the *wavefunction* describing the behavior of electrons.  $E(\mathbf{R})$  is the molecule’s energy.

Conceptually, (B1) can be used to study almost any chemical reaction in the universe without performing an experiment in a laboratory. However, the Schrödinger equation (B1) asks the computer to find a function  $\Psi(\mathbf{r}_e)$  from the collection of all the functions living in the high-dimensional space  $\mathbb{R}^{3N}$  formed by all possible electron positions, causing the search space to exponentially explode as the system size  $N$  grows. For a simple molecule with around 100 electrons, it is estimated to take longer than the age of the universe on world’s most advanced supercomputers.

To circumvent this curse of dimensionality in (B1), one strategy is to approximate  $\Psi(\mathbf{r}_e)$  as products of independent low-dimensional functions (anti-symmetrized by some operator  $\hat{P}$ ):

$$\Psi(\mathbf{r}_e) \approx \hat{P} \psi_1(\vec{r}_1) \cdot \psi_2(\vec{r}_2) \cdots \psi_{N-1}(\vec{r}_{N-1}) \cdot \psi_N(\vec{r}_N) \quad (\text{B2})$$

which is taken by many conventional quantum chemistry methods for almost a century [60], and one popular variant in this family is the density function theory (DFT). As one can expect, when using the product state approximation (B2) the predicted energy of the molecular system  $E(\mathbf{R})$  will be less accurate. While in most cases this loss of accuracy is fortunately tolerable, those conventional methods such as DFT still have at least  $\mathcal{O}(N^3)$  scaling and require fine discretization in their practical setups. In today’s scientific and industrial applications like discovering new drugs or new battery materials, it is typically required to solve the energy  $E(\mathbf{R})$  either for thousands of atoms or for millions of time stamps; therefore, conventional methods including DFT are not practical for such large-scale applications.

As another strategy, one may completely disregard  $\Psi(\mathbf{r}_e)$  and aim to empirically construct a function  $E_\theta(\mathbf{R})$  to approximate the energy  $E(\mathbf{R})$ , solely based on the atomic nuclei positions  $\mathbf{R}$ :

$$E(\mathbf{R}) \approx E_\theta(\mathbf{R}) \quad (\text{B3})$$

(B3) has been known as determining a molecule’s ‘force-field’ since the 1960s [61] which has involved countless efforts from domain experts, and has motivated recent machine learning works attempting to construct  $E_\theta(\mathbf{R})$  from data. While simulating molecules based on this strategy (B3) is usually orders-of-magnitudes faster than conventional quantum chemistry methods such as DFT, it requires either extensive domain expertise to parameterize it (for force-fields) or large amount of data (for machine learning) to train the model to the desired accuracy. They are also found to be inaccurate and lack robustness when applied to down-stream tasks out of their training distributions. Since they are purely empirical and are unaware of quantum interaction carried by electrons ( $\mathbf{r}_e$  in  $\Psi(\mathbf{r}_e)$ ), it is not surprising to find such shortcomings.

The gap between quantum chemistry approximations as in (B2) and data-driven approximations (B3) must be bridged to simultaneously satisfy the speed, accuracy and data efficiency requirements in real-world molecular modelling applications. We aim at constructing a tensorial molecular representation  $\mathbf{T}[\Psi_0]$  from a low-cost *coarse-grained wavefunction*  $\Psi_0(\mathbf{r}_e; \mathbf{R})$  to encode the quantum interaction

---

<sup>4</sup>We trade off strictness of physics for a more intuitive introduction. More rigorous and comprehensive reviews on this topic can be found in articles and textbooks, such as [59].

among atoms and electrons in a molecular system, then construct a data-driven map  $\hat{\mathcal{F}}_\theta[\mathbf{T}[\Psi_0]]$  mapping  $\mathbf{T}[\Psi_0]$  to the target  $\mathbf{y}$ . We will see that  $\mathbf{T}[\Psi_0]$  can be classified as 2-body tensors.

For molecular systems,  $\Psi_0(\mathbf{r}_e; \mathbf{R})$  can be naturally represented in *atomic orbitals*. To introduce this representation, we briefly summarize the symbolic conventions commonly employed in quantum mechanics.

**Definition B1 (Dirac’s Bra-Kets.)** Let  $V$  be a Hilbert space over  $\mathbb{C}$ . For  $u, v \in V$ , their Hermitian inner product is denoted by  $\langle u|v\rangle$ . We call  $|v\rangle$  a ket and  $\langle u|$  a bra. When  $V$  is a finite dimensional vector space, a bra  $\langle u|$  can be thought as a row vector and a ket  $|v\rangle$  as a column vector.

In physicist’s convention  $|v\rangle$  is referred to as a quantum state. In this section we restrict ourselves to single-electron quantum states in the real space  $\mathbb{R}^3$ , where the Hilbert space is the function space of square-integrable functions:  $V = L^2(\mathbb{R}^3)$ . In this setting the inner product is given by  $\langle u|v\rangle = \int_{\mathbb{R}^3} u^*(\mathbf{r})v(\mathbf{r})d\mathbf{r}$  where  $u^*(\mathbf{r})$  denotes the complex conjugation of  $u(\mathbf{r})$ .

**Definition B2 (quantum operators.)** A (single-electron-reduced) quantum operator  $\hat{O} : V \rightarrow V$  is a self-adjoint linear operator.  $\hat{O}|u\rangle$  denotes the quantum operator acting on a ket vector. Given a set of kets  $\{|\phi_i\rangle\}$ ,  $O_{ij} := \langle \phi_i|\hat{O}|\phi_j\rangle$  is called a matrix representation of  $\hat{O}$ .

**Definition B3 (Atomic orbitals.)** An atomic orbital  $|\Phi_A^{n,l,m}\rangle$  takes the functional form  $\Phi_A^{n,l,m}(\mathbf{r}) := R_{n,l}^{z_A}(\|\mathbf{r} - \mathbf{R}_A\|)Y_{lm}(\frac{\mathbf{r}-\mathbf{R}_A}{\|\mathbf{r}-\mathbf{R}_A\|})$ , where  $\mathbf{R}_A$  is the nuclear position of atom A,  $z_A$  denotes the atomic number of atom A,  $R_{n,l}^{z_A}$  is called a radial function and does not depend on the direction of  $\mathbf{r} - \mathbf{R}_A$ , and  $Y_{lm}$  is a spherical harmonic of degree  $l$  and order  $m$  (not to be confused with the order of  $N$ -body tensors). For hydrogen-like atoms  $\Phi_A^{n,l,m}(\mathbf{r})$  with certain forms of  $R_{n,l}^{z_A}(\mathbf{r})$  are known as the exact wavefunction solution of (B1), and for molecular systems they are employed as the basis functions to numerically represent the many-electron wavefunction. It should be stressed that in most cases, the collection of atomic orbitals are neither mutually orthogonal nor a complete basis of  $V$ , but serves as a computationally tractable representation basis of  $\Psi(\mathbf{r}_e; \mathbf{R})$ . The particular choice of  $R_{n,l}$  has been the subject of decades of research [62–64]. See Appendix B.2 for the parameterization of  $\Phi_A^{n,l,m}(\mathbf{r})$  in our settings.

For the set of kets given by atomic orbitals  $\{|\Phi_A^{n,l,m}\rangle\}$  of a molecule, we use  $\mathbf{O}$  to denote the matrix representation of a quantum operator  $\hat{O}$  in  $\{|\Phi_A^{n,l,m}\rangle\}$ , which is by definition a 2-body tensor with the adaptation of notations  $\mathbf{T} := \mathbf{O}$ ,  $\vec{u} := (A, B)$  and  $\vec{v} := (n_A, l_A, m_A; n_B, l_B, m_B)$ .

We featurize the molecule by such a 2-body tensor representation  $\mathbf{O}[\Psi_0]$  built from an coarse-grained wavefunction  $\Psi_0(\mathbf{r}_e; \mathbf{R})$  and the atomic orbitals  $\{|\Phi_A^{n,l,m}\rangle\}$  of the given molecule. The quantum operators  $\hat{O}[\Psi_0]$  corresponding to the coarse-grained wavefunction  $\Psi_0$  are efficiently computed via a *Tight-binding Hamiltonian*, as detailed in Appendix B.2. We emphasize that the required computational time to generate  $\hat{O}[\Psi_0]$  is at least  $10^3$ -fold lower than obtaining the ground-truth (e.g. a DFT calculation), and the resulting 2-body tensor representation  $\mathbf{O}[\Psi_0]$  is infinitely differentiable (e.g. with respect to atom coordinates  $\mathbf{R}$  or external electric/magnetic fields).

## B.2 The employed tensorial molecular representation and its back-propagation

The tensor-based molecular representation employed in this work is motivated by a pair of recent works [35, 65], but we directly construct the features using atomic orbitals without the need of compute-intensive post-processing algorithms to enforce rotational invariance in contrast to their method. Ours can be also used to predict tensor-valued quantities.

In particular, this work (as well as [35] and [65]) constructs features based on the GFN1-xTB semi-empirical electronic structure method [66]. As a member of the class of *mean field* or *self-consistent field* quantum chemical methods, GFN1-xTB centers around the self-consistent solution of the Roothaan-Hall equations,

$$\mathbf{FC} = \mathbf{SC}\epsilon. \tag{B4}$$

All boldface symbols are matrices (i.e. 2-tensors) represented in an atomic orbital basis. For the particular case of GFN1-xTB, this basis is called STO-6G and comprises a set of hydrogen-like orbitals approximated as sums of gaussian functions multiplied by polynomials.  $\mathbf{C}$  is a compact representation of the wavefunction  $\Psi_0$  of (B2).  $\epsilon$  is a diagonal eigenvalue matrix.  $\mathbf{S}$  is the *overlap matrix* and is given by

$$S_{\mu\nu} = \langle \mu | \nu \rangle \quad (\text{B5})$$

where  $\mu$  and  $\nu$  index the atomic orbital basis.  $\mathbf{F}$  is the *Fock matrix* and is given by

$$\mathbf{F} = \mathbf{h} + \mathbf{G}[\mathbf{P}]. \quad (\text{B6})$$

$\mathbf{h}$  is the *one-electron integrals*, and includes electron-nuclear attraction and electron kinetic energy.  $\mathbf{G}$  is the *two-electron integrals*, and comprises the electron-electron repulsion. Approximation of  $\mathbf{G}$  is the key task for self-consistent field methods, and GFN1-xTB provides an accurate and efficient approximation for  $\mathbf{G}$ . Finally,  $\mathbf{P}$  is the (one-electron) *density matrix*, and is given by

$$P_{\mu\nu} = \sum_{i=1}^{n_{\text{elec}}/2} C_{\mu i}^* C_{\nu i}. \quad (\text{B7})$$

$n_{\text{elec}}$  is the number of electrons, and a closed-shell singlet ground state is assumed for simplicity.

Equations B4 and B6 are solved for  $\mathbf{P}$ .

The electronic energy,  $E(\mathbf{R})$ , is related to the Fock matrix by

$$\mathbf{F} = \frac{\delta E(\mathbf{R})}{\delta \mathbf{P}}. \quad (\text{B8})$$

The particular form of the GFN1-xTB electronic energy may be found in [66].

UNiTE is trained to predict the the quantum chemistry properties of a more accurate and expensive electronic structure method (such as DFT) based on  $\mathbf{O} := [\mathbf{F}, \mathbf{P}, \mathbf{S}, \mathbf{h}]$ . For the example of electronic energy,

$$E_{\text{DFT}}(\mathbf{R}) \approx E_{\text{TB}}(\mathbf{R}) + E_{\text{UNiTE}}(\mathbf{O}). \quad (\text{B9})$$

Note that  $\mathbf{F}$ ,  $\mathbf{P}$ ,  $\mathbf{S}$ , and  $\mathbf{h}$  all implicitly depend on  $\mathbf{R}$ .

In addition to predicting  $E(\mathbf{R})$ , it is also useful to predict its gradient with respect to nuclear coordinates. For example, the nuclear gradient may be used to simulate molecular motion at finite temperature, or to find representative *equilibrium* geometries by locally minimizing  $E(\mathbf{R})$  (e.g. in the geometry optimization benchmark of Table 2). Rather than learning the gradient separately from the energy, we directly differentiate the learned energy (B9). The partial derivative of the UNiTE energy with respect to  $\mathbf{F}$ ,  $\mathbf{P}$ ,  $\mathbf{S}$ , and  $\mathbf{h}$  is determined through automatic differentiation (as with the backpropagation of the loss during training). The partial derivatives of  $\mathbf{F}$ ,  $\mathbf{P}$ ,  $\mathbf{S}$ , and  $\mathbf{h}$  with respect to  $\mathbf{R}$  are computed following Appendix D of [65], with the simplification that the SAAO transformation matrix  $\mathbf{X}$  is replaced by the identity.

### B.3 Parameterization of the Wigner-Eckart layer

Starting from this subsection, we restrict the group to  $O(3)$  which is the group of rotating/reflecting atomic orbitals in the molecular representation (see Definition B1). Their irreducible representations are labelled as  $L := (l, p)$  and  $M := m$  to parallel the commonly used convention for spherical harmonics  $Y_{lm}$  and Clebsch-Gordan coefficients, as discussed in (A9).

For quantum chemistry tasks, we employ a physically-motivated scheme to efficiently construct  $\mathbf{Q}$  defined in Lemma 1 for decomposing the diagonal sub-tensors of  $\mathbf{O}$ , i.e. the 2-body tensor molecular representation:

$$\tilde{Q}_{n,l,m}^{\vec{v}} := \tilde{Q}_{nlm}^{n_1,l_1,m_1;n_2,l_2,m_2} = \int_{\mathbf{r} \in \mathbb{R}^3} \Phi_A^{n_1,l_1,m_1}(\mathbf{r}) \Phi_A^{n_2,l_2,m_2}(\mathbf{r}) (\tilde{\Phi}_A^{n,l,m}(\mathbf{r}))^* d\mathbf{r} \quad (\text{B10})$$

where  $\Phi_A$  are atomic orbital basis, and  $\tilde{\Phi}_A$  are constructed as products of Gaussian functions and real spherical harmonics, defined as (for conciseness, at  $\mathbf{R}_A = 0$ ):

$$\tilde{\Phi}^{n,l,m}(\mathbf{r}) := c_{n,l} \cdot \exp(-\gamma_{n,l} \cdot r^2) r^l Y_{lm}\left(\frac{\mathbf{r}}{r}\right) \quad (\text{B11})$$

where  $c_{n,l}$  is a normalization constant such that  $\int_{\mathbf{r}} \|\tilde{\Phi}_A^{n,l,m}(\mathbf{r})\|^2 d\mathbf{r} = 1$  following the conventions of ‘Gaussian basis functions’ [67]. For numerical experiments considered in this work, the scale parameters  $\gamma$  are heuristically chosen as (in atomic units):

$$\begin{aligned}\gamma_{n,l=0} &:= 128 \cdot (0.5)^{n-1} \quad \text{where } n \in \{1, 2, \dots, 16\} \\ \gamma_{n,l=1} &:= 32 \cdot (0.25)^{n-1} \quad \text{where } n \in \{1, 2, \dots, 8\} \\ \gamma_{n,l=2} &:= 4.0 \cdot (0.25)^{n-1} \quad \text{where } n \in \{1, 2, 3, 4\}\end{aligned}$$

The constructed  $\tilde{\mathbf{Q}}$  satisfies equivariance constraints on  $\mathbf{Q}$  due to their relations to  $SO(3)$  Clebsch-Gordan coefficients  $C_{l_1 m_1; l_2 m_2}^{lm} \propto \int_{\mathbf{r} \in \mathbb{R}^3} Y_{l_1 m_1}(\mathbf{r}) Y_{l_2 m_2}(\mathbf{r}) (Y_{lm}(\mathbf{r}))^* d\mathbf{r}$  [10]. We note that for molecular representations, this parameterization of the Wigner-Eckart layer  $\psi$  based on (B10) naturally handles the subtlety that atomic orbitals  $\Phi_A$  are usually parameterized differently for each chemical element, by projecting to the auxiliary basis  $\tilde{\Phi}_A$  which do not depend on the atomic numbers. In practice  $\tilde{\mathbf{Q}}$  can be efficiently tabulated using existing programs such as [68].

The resulted embeddings  $\mathbf{h}_A$ , in its explicit form

$$\begin{aligned}\mathbf{h}_A &:= \bigoplus_{n,l,p,m} (h_A)_{n,l,p,m} \quad \text{where} \\ (h_A)_{n,l,(p=1),m} &:= \sum_{\vec{v}} (\mathbf{O}_{AA})^{\vec{v}} \tilde{\mathbf{Q}}_{n,l,m}^{\vec{v}} = \sum_{n_1, l_1, m_1} \sum_{n_2, l_2, m_2} \langle \Phi_A^{n_1, l_1, m_1} | \hat{O} | \Phi_A^{n_2, l_2, m_2} \rangle \tilde{Q}_{nlm}^{n_1, l_1, m_1; n_2, l_2, m_2} \\ (h_A)_{n,l,(p=-1),m} &:= 0\end{aligned}$$

are then transformed by a point-wise interaction block (Equations 9-11) as the initial order-1 representations,  $\mathbf{h}^{t=0}$ , to pass into UNiTE blocks.

## B.4 Physics-informed pooling schemes for quantum chemical properties

We define schemes for learning different classes of chemical properties  $\mathbf{y} \in \mathcal{Y}$  without a need of modifying the base architecture of UNiTE. We use  $A$  to denote an atom index,  $|A|$  to denote the total number of atoms in the molecule,  $z_A \in \mathbb{N}^+$  to denote the atomic number of atom  $A$ , and  $\vec{R}_A \in \mathbb{R}^3$  to denote the atomic nuclei coordinate of atom  $A$ .

### B.4.1 Scalar-valued extensive quantities

A representative target in this family is the molecular electronic energy  $E(\mathbf{R})$  (i.e.,  $U_0$  in the convention of QM9), which is rotation-invariant and grows when increasing the system size (extensive). We use the following pooling operation:

$$y_\theta = \sum_A \mathbf{W}_o \cdot \|\mathbf{h}_A^{t_f}\| + b_{z_A}^o \quad (\text{B12})$$

where  $\mathbf{W}_o$  is a learnable linear layer and  $b_{z_A}^o$  are learnable biases for each atomic number  $z$ . To account for nuclei contributions to molecular energies (which can be thought as as function of  $\{z_A\}$ ), we initialize  $b_z^o$  from a linear regression on the targets  $y$  based on  $\{z_A\}$  to speed up training on those tasks. This scheme is employed for learning  $U_0, U, H, G, \text{ZPVE}$  and  $c_v$  on QM9, for the energies part in MD17 and for the model described in Section 5.4. For  $U_0, U, H, G$  which are quantities derived from  $E(\mathbf{R})$ , we also initialized the model outputs as the tight-binding approximated electronic energy  $E_{\text{TB}}(\mathbf{R})$  (which is a known analytic function of  $\mathbf{O}$  and  $\mathbf{R}$  readily available at featurization time, see [66]) to precondition the learning problem. Test MAEs on QM9 without employing this preconditioning strategy are also provided for reference (“direct learning” in Figure 3(a)).

### B.4.2 Dipole moment $\vec{\mu}$

The dipole moment  $\vec{\mu}$  can be thought as a vector in  $\mathbb{R}^3$ . It is modelled as a combination of atomic charges  $q_u$  and atomic dipoles  $\vec{\mu}_u$ , and the pooling operation is defined as

$$\vec{\mu}_\theta = \sum_A (\vec{R}_A \cdot q_A + \vec{\mu}_A) \quad (\text{B13})$$

$$q_A = q'_A - \Delta q \quad \text{where} \quad \Delta q := \frac{\sum_A q'_A}{|A|} \quad (\text{B14})$$

$$q'_A := \mathbf{W}_{o,0} \cdot (\mathbf{h}_A^{t_f})_{l=0,p=1} + b_{z_A}^o \quad (\text{B15})$$

$$(\vec{\mu}_A)_m := \mathbf{W}_{o,1} \cdot (\mathbf{h}_A^{t_f})_{l=1,p=1,m} \quad \text{where} \quad m \in \{x, y, z\} \quad (\text{B16})$$

where  $\mathbf{W}_{o,0}$  and  $\mathbf{W}_{o,1}$  are learnable linear layers. Note that (B14) ensures the translation invariance of the prediction. Similar to the strategy applied to electronic energies, we use the tight-binding approximated dipole moment  $\vec{\mu}_{\text{TB}}$  to initialize the model outputs, and test MAEs without this preconditioning are also provided for reference (“direct learning” in Figure 3(b)).

Note that UNiTE is trained by directly minimizing a loss function  $\mathcal{L}(\vec{\mu}, \vec{\mu}_\theta)$  between the ground truth and the predicted molecular dipole moment vectors. For the published QM9 reference labels [30] only the dipole norm  $\mu := \|\vec{\mu}\|$  is available; we use the same pooling scheme to readout  $\vec{\mu}_\theta$  but train on  $\mathcal{L}(\mu, \|\vec{\mu}_\theta\|)$  instead.

### B.4.3 Polarizibility $\alpha$

The pooling operation for isotropic polarizibility  $\alpha$  is defined as

$$\alpha_\theta = \sum_A (\alpha_A + \vec{R}_A \cdot \vec{p}_A) \quad (\text{B17})$$

$$\alpha_A := \mathbf{W}_{o,0} \cdot (\mathbf{h}_A^{t_f})_{l=0,p=1} + b_{z_A}^o \quad (\text{B18})$$

$$\vec{p}_A = \vec{p}'_A - \Delta \vec{p} \quad \text{where} \quad \Delta \vec{p} := \frac{\sum_A \vec{p}'_A}{|A|} \quad (\text{B19})$$

$$(\vec{p}'_A)_m := \mathbf{W}_{o,1} \cdot (\mathbf{h}_A^{t_f})_{l=1,p=1,m} \quad \text{where} \quad m \in \{x, y, z\} \quad (\text{B20})$$

which is in spirit similar to the pooling scheme for  $\vec{\mu}$ .

### B.4.4 Molecular orbital properties

Molecular orbital (MO) properties, especially the energies of the highest occupied molecular orbital (HOMO), the lowest unoccupied molecular orbital (LUMO) and HOMO-LUMO gaps are important quantum-chemical properties with known implications on chemical reactivity and catalysis [69]. However, we claim that point-cloud- or graph-based descriptors are fundamentally not sufficient for learning such properties associated with individual MOs, since the target MOs are by definition localized in the electron energy space (and are often spatially localized as well) which cannot be trivially addressed by  $\mathbf{R}$ -based descriptors which typically treats all atoms equivalently. Furthermore, MO energies are intensive when varying the system sizes. Therefore, a qualitatively correct description for learning MO properties such as HOMO-LUMO gaps requires breaking the spatial degeneracy within the molecular representation, and the neural network outputs need to be size-intensive.

For proof-of-principle purposes, in this study we supplied the following tight-binding-orbital-derived features  $\mathbf{D}^{k_{\text{occ}}}$  and  $\mathbf{D}^{k_{\text{vir}}}$  to the molecular representation  $\mathbf{O}$  additional to the  $\mathbf{F}$ ,  $\mathbf{P}$ ,  $\mathbf{S}$ ,  $\mathbf{h}$  described in Section B.2, to improve the description on the locality of molecular orbitals, defined as:

$$D_{\mu\nu}^{k_{\text{occ}}} = \sum_i C_{i\mu} C_{i\nu} \cdot \exp(-k_{\text{occ}} \cdot (\epsilon_{\text{HOMO}} - \epsilon_i)) \cdot n_i \quad (\text{B21})$$

$$D_{\mu\nu}^{k_{\text{vir}}} = \sum_i C_{i\mu} C_{i\nu} \cdot \exp(-k_{\text{vir}} \cdot (\epsilon_i - \epsilon_{\text{LUMO}})) \cdot (1 - n_i) \quad (\text{B22})$$

where  $\epsilon_i$  and  $n_i$  are the orbital energy and occupation number of the  $i$ -th tight-binding orbital. In this work we heuristically choose  $k_{\text{occ}} \in \{4, 16, 64, 256\}$  and  $k_{\text{vir}} \in \{4, 16, 64, 256\}$  (in atomic units) without hand-tuning  $k_{\text{occ}}$  and  $k_{\text{vir}}$ . In the pooling layer of UNiTE, we design the following *global-attention* based pooling to produce size-intensive predictions:

$$a_A = \text{Softmax}(\mathbf{W}_a \cdot \|\mathbf{h}_A^{t_f}\|) := \frac{\mathbf{W}_a \cdot \|\mathbf{h}_A^{t_f}\|}{\sum_A \mathbf{W}_a \cdot \|\mathbf{h}_A^{t_f}\|} \quad (\text{B23})$$

$$y_\theta = \sum_A a_A \cdot (\mathbf{W}_o \cdot \|\mathbf{h}_A^{t_f}\| + b_{z_A}^o) \quad (\text{B24})$$

where  $\mathbf{W}_a$  and  $\mathbf{W}_o$  are learnable linear layers and  $b_{z_A}^o$  are learnable biases for each atomic number  $z$ . Similar to energy tasks, we initialize  $b_z^o$  from a linear fitting on the targets to precondition training.

We take the difference between the predicted HOMO energies ( $\epsilon_{\text{HOMO}}$ ) and LUMO energies ( $\epsilon_{\text{LUMO}}$ ) as the HOMO-LUMO Gap ( $\Delta\epsilon$ ) predictions. As shown in Table 1, we find UNiTE together with this choice of molecular representation achieves significant improvements when compared previous ML approaches at predicting  $\epsilon_{\text{HOMO}}$ ,  $\epsilon_{\text{LUMO}}$ , and  $\Delta\epsilon$ . We note that it is also possible to construct a framework to learn MO properties by directly taking the tight-binding MO coefficients  $\mathbf{C}$  (defined in (B4)) as features, which requires extending the UNiTE implementation to group  $U(1) \times O(3)$  to be equivariant to orbital phase symmetries, and is left as a direction for future works.

#### B.4.5 Electronic spatial extent $\langle R^2 \rangle$

The pooling scheme for  $\langle R^2 \rangle$  is defined as:

$$\langle R^2 \rangle_\theta = \sum_A (||\vec{R}_A - \vec{R}_0||^2 \cdot q_A + s_A) \quad (\text{B25})$$

$$\vec{R}_0 := \frac{\sum_A (\vec{R}_A \cdot q_A + \vec{\mu}_A)}{\sum_A q_A} \quad (\text{B26})$$

$$q_A := \mathbf{W}_{o,0} \cdot (\mathbf{h}_A^{t_f})_{l=0,p=1} + b_{z_A}^o \quad (\text{B27})$$

$$(\vec{\mu}_A)_m := \mathbf{W}_{o,1} \cdot (\mathbf{h}_A^{t_f})_{l=1,p=1,m} \quad \text{where } m \in \{x, y, z\} \quad (\text{B28})$$

$$s_A := \mathbf{W}_{o,2} \cdot (\mathbf{h}_A^{t_f})_{l=0,p=1} \quad (\text{B29})$$

where  $\mathbf{W}_{o,0}$ ,  $\mathbf{W}_{o,1}$  and  $\mathbf{W}_{o,2}$  are learnable linear layers.

#### B.4.6 Electron densities $\rho(\vec{r})$

Both the ground truth and predicted electron densities  $\rho(\vec{r})$  are represented in a set of atomic-orbital-like, so called *density fitting* basis  $\{\Phi^\rho\}$ :

$$\rho(\vec{r}) = \sum_A \sum_{\nu_A l m} (\Phi_A^{\nu_A l m}(\vec{r}) \cdot d_A^{\nu_A l m} \quad \text{where } \nu_A \in \{\nu\}_{z_A} \quad (\text{B30})$$

which is similar to the approach employed in [42]. The details on the definition of  $\{\Phi^\rho\}$  and the procedure to compute the density coefficients  $d_A^{\nu_A l m}$  are given in Appendix F.2. For the focus here, we define the pooling operation to predict  $\rho(\vec{r})$  from UNiTE:

$$(d_\theta)_A^{\nu_A l m} = (\mathbf{W}_{z_A, l}^d \cdot (\mathbf{h}_A^{t_f})_{l,p=1,m})_{\nu_A} \quad (\text{B31})$$

where  $\mathbf{W}_{z,l}^d$  are learnable linear layers with weights specific to each chemical element  $z$  and representation index  $l$ . This atom-centered expansion scheme compactly parameterizes the predicted density  $\rho_\theta(\vec{r})$ . We emphasize that all the parameters in UNiTE, except for this density pooling layer, do not depend on the atomic numbers  $z$ .

## C Technical aspects and model implementation

**Efficient GPU evaluation of spherical harmonics and Clebsch-Gordan coefficients.** In our implementation, all the operations related to group representations of  $O(3)$  are realized through element-wise operations and gather-scatter operations on arrays, without the need of recursive computations at runtime that are difficult to parallelize on GPUs. The real spherical harmonics (RSHs) are computed based on Equations 6.4.47-6.4.50 of [70], which only requires computing element-wise powers on arrays and a linear combination with pre-tabulated coefficients. The Clebsch-Gordan (CG) coefficients are first tabulated using their explicit expressions for complex spherical harmonics (CSHs) based on Equation 3.8.49 of [10], and are then transformed to RSH CG coefficients with the transformation matrix between RSHs and CSHs [71]. We also claim our strategy to be better scalable to physical spaces of higher dimensions.

**Multiple input channels.** UNiTE can be directly extended to  $N$ -body tensors that have extra feature dimensions, through applying a learnable linear layer  $\mathbf{W}^{\text{in}}$  ("Linear" in Figure 3) to transform and fold them into a fixed-size channel dimension. Each channel is then shared among a subset of convolution channels (indexed by  $i$ ), instead of using one convolution kernel for all channels  $i$ .

For example, the tensorial molecular representations  $\mathbf{O}$  introduced in Section B.2 is a stack of 2-body tensors; for the numerical experiments of this work, they are mixed into  $\mathcal{N}^{\text{in}}$  input channels by  $\mathbf{W}^{\text{in}}$  and we assign a convolution channel to each input channel.

**Parameterization of  $\alpha_{\bar{u}}^t$ .** In general  $\alpha_{\bar{u}}^{t,j}$  may be constructed by equivariant extensions of existing set-to-scalar models such as Deep Sets [72] depending on the actual learning problem setup. In a case where  $G_u = O(n)$ ,  $N = 2$  and the local reference frames can be aligned with a global coordinate system (e.g. in the quantum chemistry tasks considered in this study), we propose to parameterize  $\alpha_{\bar{u}}^t := \alpha_{AB}^t$  as *equivariant multi-head attentions*:

$$\alpha_{AB}^t = \text{MLP}\left(\left(\mathbf{z}_{AB}^t \cdot \mathbf{W}_\alpha^t\right) \odot \kappa\left(\|\mathbf{T}_{AB}\|\right) / \sqrt{n_\alpha}\right) \quad \text{where} \quad \mathbf{z}_{AB}^t = \bigoplus_{n,l,p} \sum_{m=-l}^l (h_A^t)^{n,l,m,p} \cdot (h_B^t)^{n,l,m,p} \quad (\text{C1})$$

where MLP denotes a 2-layer MLP,  $\mathbf{W}_\alpha^t$  are learnable linear functions and  $n_\alpha$  denotes the number of attention heads (i.e. length of  $\mathbf{a}_{AB}^t$ ).  $\kappa(\cdot)$  can be chosen as a set of radial basis functions shared across all update steps  $t$ , and its functional form may be determined based on the application domain. For the learning tasks of interest in this work, we use Morlet wavelet basis functions for  $\kappa$ :

$$\kappa\left(\|\mathbf{T}_{AB}\|\right) := \mathbf{W}_\kappa\left(\bigoplus_k \sum_{n_A, l_A} \sum_{n_B, l_B} \xi^k\left(\log\left(\|\mathbf{T}_{AB}^{n_A, l_A; n_B, l_B}\|\right)\right)\right) \quad (\text{C2})$$

$$\xi^k(x) := \exp(-\gamma_k \cdot x^2) \cdot \cos(\pi \gamma_k \cdot x) \quad (\text{C3})$$

where  $\mathbf{W}_\kappa^t$  are learnable linear functions and  $n_\alpha$  denotes the number of attention heads (i.e. length of  $\mathbf{a}_{AB}^t$ ), and  $\gamma_k$  are learnable frequency coefficients initialized as  $\gamma_k = 0.3 \cdot (1.08)^k$  where  $k \in \{0, 1, \dots, 15\}$  in this work. The attention mechanism (C1) improves the network capacity without increasing memory costs as opposed to explicitly expanding  $\mathbf{T}$ , which in spirit coincides with a scheme recently proposed in SE(3)-transformers [11].

**Restricted summands in Clebsch-Gordan coupling.** For computational efficiency, in the Clebsch-gordan coupling (10) (i.e., (A18)) of a point-wise interaction block, we further restrict the angular momentum indices  $(l_1, l_2)$  within the range  $\{(l_1, l_2); l_1 + l_2 \leq l_{\max}, l_1 \leq n, l_2 \leq n\}$  where  $l_{\max}$  is the maximum angular momentum considered in the implementation.

**Incorporating geometric information.** For quantum chemistry tasks, the point cloud of atomic nuclei coordinates  $\mathbf{R}$  is also known in addition to the tensorial molecular representation  $\mathbf{T}$ . In that case, we can feasibly incorporate the geometric information of atom center positions  $\mathbf{R}$  through spherical harmonics, with the following modified message-passing scheme to extend (4):

$$(\tilde{\mathbf{m}}_A^t)_{lm} = \sum_{B \neq A} \bigoplus_{i,j} \left( (\mathbf{m}_{AB}^{t,i})_{lm} + Y_{lm}(\hat{R}_{AB}) \left( \mathbf{W}_{R,i}^{l,t} \|\mathbf{m}_{AB}^{t,i}\| \right) \right) \cdot \alpha_{AB}^{t,j} \quad (\text{C4})$$

Table D1: The model hyperparameters for UNiTE used in this work.

Symbol	Meaning	Defined in	Value(s)
$\mathcal{N}^h$	Total number of feature channels in $\mathbf{h}^t$	Sec. A.3, (6)	256
$\mathcal{N}_{lp}^h$	Number of feature channels for each representation group $(l, p)$ in $\mathbf{h}^t$	Sec. A.3, (6)	See Table D2
$t_1$	Number of convolution-message-passing update steps	Sec. 4	4
$t_2$	Number of post-update point-wise interaction blocks	Sec. 4	4
$\mathcal{N}^{\text{in}}$	Number of input channels	Sec A.8.1	8
$\mathcal{N}^i$	Number of convolution channels $i$	(A11) i.e. (3), Sec. A.3	8
$\mathcal{N}^j$	Number of attention heads $j$	(A12) i.e. (4), Sec. A.3	8
$d^{\text{MLP}}$	Depth of MLPs	MLPs in (9)-(11)	2
$\sigma$	Activation function	MLPs in (9)-(11)	Swish [73]
$\mathcal{N}^\xi$	Number of Radial basis functions $\xi$	(C3)	16
	Estimation scheme for $(\mu, \sigma)$ for EvNorm in a point-wise interaction block during updates	(A14) i.e. (8)	BatchNorm [28]
	Estimation scheme for $(\mu, \sigma)$ for EvNorm in post-update point-wise interaction blocks	(A14) i.e. (8)	LayerNorm [29]
	Initialization of $\beta_{nlp}$ in EvNorm layers	(A14) i.e. (8)	Uniform $([0.5, 1.5])$
$\epsilon$	Stability factor in EvNorm layers	(A14) i.e. (8)	0.01
	Total number of parameters	-	2.1M

where  $\hat{R}_{AB} := \frac{\vec{R}_{AB}}{\|\vec{R}_{AB}\|}$  denotes the direction vector between atomic centers A and B, and  $\mathbf{W}_{R,i}^{l,t}$  are learnable linear functions.

**Matching layers.** For this implementation, the operations of matching layers  $\rho$  and  $\rho^\dagger$  are then simply to ‘drop’ or ‘zero-pad’ the  $p = -1$  components to  $\mathbf{h}^t$ , since the atomic orbitals used for define the 2-body tensor  $\mathbf{O}$  are basis of  $\text{SO}(3)$  and do not contain negative parity components.

**Time complexity.** The asymptotic time complexity of our model is  $\mathcal{O}(BN^3t_1 + dC)$ , where  $d$  denotes the size of each dimension of  $\mathbf{T}$ ,  $B$  denotes the number of non-zero entries in  $\mathbf{T}$ , and  $C$  denotes the number of elements in each diagonal sub-tensor  $\mathbf{T}_v$ .

## D Hyperparameters and training setups

### D.1 Model hyperparameters

We use the same set of model hyperparameters to obtain all numerical experiment results on open benchmarks reported in this work. The hyperparameters employed in this work are summarized in Table D1 and Table D2. The model used for zero-shot generalization on down stream chemistry tasks also employs this set of hyperparameters with the only difference of using LayerNorm [29] for mean  $\mu$  and variance  $\sigma$  estimates in all EvNorm layers. This choice is made to improve model robustness when applied to extrapolative molecular geometries which can be thought as adversarial samples.

### D.2 Training

For all training setups we use the Adam optimizer [74] with maximal learning rate  $5 \times 10^{-4}$  and parameters  $\beta_1 = 0.9, \beta_2 = 0.999$  and  $\epsilon = 10^{-4}$ . The loss function denoted as  $\mathcal{L}$  below refers to a

Table D2: The number of feature channels  $\mathcal{N}_{lp}^h$  for each representation group  $(l, p)$  of  $\mathbf{h}^t$  used in this work across all values of  $t$ . Note that  $l_{\max} = 4$ .

$\mathcal{N}_{lp}^h$	$l = 0$	$l = 1$	$l = 2$	$l = 3$	$l = 4$
$p = +1$	128	48	24	12	6
$p = -1$	24	8	4	2	0

SmoothL1Loss function [75]. Batch sizes and the total number of epochs are adjusted for different benchmarks to account for their vastly different training set sizes, as detailed below. We did not employ additional regularization techniques such as weight decay or early stopping.

**QM9.** For QM9 tasks we optimize the model using the loss  $\mathcal{L}(y, y_\theta)$  for each target  $y$ . We use a batch size of 64 when the training sample size  $> 1000$ , and a batch size of 16 for smaller training sizes. We employ a learning rate schedule of first performing linear warmup for 100 epochs to the maximal learning rate followed by a cosine learning rate annealing [76] for 200 epochs. Models are trained on a single Nvidia Tesla V100-SXM2-32GB GPU, taking around 36 hours for training runs with 110k training samples.

**MD17.** For MD17, we optimize the model by simultaneously training on energies  $E(\mathbf{R})$  and forces  $\mathbf{F}(\mathbf{R})$ , using the following loss function:

$$\mathcal{L}_{E+\mathbf{F}}(E, \mathbf{F}; E_\theta, \mathbf{F}_\theta) := \mathcal{L}(E(\mathbf{R}); E_\theta(\mathbf{R})) + c_F \cdot \frac{1}{3|A|} \sum_A \sum_{m \in \{x, y, z\}} \mathcal{L}\left(-\frac{\partial E_\theta(\mathbf{R})}{\partial R_{A,m}} - F_{A,m}(\mathbf{R})\right) \quad (\text{D1})$$

Following previous works [21, 24], we set  $c_F$  to 1000 Å. For each molecule in MD17, we use the 1000 geometries of the ‘train 01’ subset given by [39] for training. We use a batch size of 8, and train the model on a single Nvidia Tesla V100-SXM2-32GB GPU for 1500 epochs using a cosine decay learning rate schedule, taking around 30 hours for each training run.

**Electron densities.** For electron density, we train on the  $L^2$  density loss

$$\mathcal{L}_\rho(\rho, \rho_\theta) := \int \|\rho(\vec{r}) - \rho_\theta(\vec{r})\|^2 d\vec{r} = (\mathbf{d} - \mathbf{d}_\theta)^T \mathbf{S}^\rho (\mathbf{d} - \mathbf{d}_\theta) \quad (\text{D2})$$

where the density coefficients  $\mathbf{d} := \bigoplus_{A, \nu_A, l, m} d_A^{\nu_A l m}$  are defined in (B30), and  $\mathbf{S}^\rho$  is the overlap matrix of the density fitting basis  $\{\Phi^\rho\}$ . A detailed derivation for the RHS of (D2) can be found in the appendix of [77]. We use a batch size of 64 and a cosine annealing learning schedule for training; we train the model on a single Nvidia Tesla V100-SXM2-32GB GPU for 2000 epochs on the BFDb-SSI dataset taking 10 hours, and for 500 epochs on the QM9 dataset taking 120 hours.

**The model for down stream chemistry tasks (Sec. 5.4).** The training dataset (see F.1) contains different geometries  $b_\eta$  for each molecule  $\eta$  in the dataset. We train on a loss function following [35]:

$$\mathcal{L}_G(E(\eta, b_\eta), E_\theta(\eta, b_\eta)) := \mathcal{L}(E(\eta, b_\eta), E_\theta(\eta, b_\eta)) + c_G \cdot \mathcal{L}(E(\eta, b_\eta) - E(\eta, \hat{b}_\eta), E_\theta(\eta, b_\eta) - E_\theta(\eta, \hat{b}_\eta)) \quad (\text{D3})$$

where  $\hat{b}_\eta$  is a geometry randomly sampled from all the geometries  $\{b_\eta\}$  of each molecule  $\eta$  within each mini-batch during training. We use  $c_G = 10$  in this work. We train the model for 125 epochs on six Nvidia Tesla V100-SXM2-32GB GPUs with data parallelism, using a total batch size of 96 and a cosine annealing learning rate schedule taking 50 hours.

## E Supplementary experimental results

### E.1 MD17 and rMD17

Table E1: Prediction force MAEs (in kcal/mol/Å) on the MD17 dataset for models trained on 1000 samples. The best results on each task are marked in bold and the second-bests are indicated by underline.

Molecule	Kernel Methods		Neural Networks				
	sGDML	FCHL19	DimeNet	NequIP ( $l = 1$ )	PaiNN	UNiTE (direct learning)	UNiTE (preconditioned)
Aspirin	0.68	0.481	0.499	<u>0.348</u>	0.371	<b>0.156</b>	0.118
Ethanol	0.33	<u>0.144</u>	0.230	0.208	0.230	<b>0.092</b>	0.069
Malonaldehyde	0.41	<u>0.237</u>	0.383	0.337	0.319	<b>0.159</b>	0.128
Naphthalene	0.11	0.150	0.215	0.096	<u>0.083</u>	<b>0.064</b>	0.048
Salicylic Acid	0.28	0.220	0.374	0.238	<u>0.209</u>	<b>0.097</b>	0.067
Toluene	0.14	0.204	0.216	<u>0.101</u>	0.102	<b>0.072</b>	0.057
Uracil	0.24	<b>0.097</b>	0.301	0.172	0.140	<u>0.098</u>	0.072

Table E2: Prediction MAEs on the revised MD17 dataset in terms of energies (in meV) and forces (in meV/Å) for models trained on 1000 samples.

Molecule		FCHL19	NequIP ( $l = 3$ )	UNiTE (direct learning)	UNiTE (preconditioned)
Aspirin	Energy	6.2	<b>2.4</b>	<b>2.4</b>	1.8
	Forces	20.9	8.1	<b>7.6</b>	6.1
Azobenzene	Energy	2.8	3.3	<b>1.1</b>	0.63
	Forces	10.8	<b>2.8</b>	4.2	2.7
Ethanol	Energy	0.9	1.2	<b>0.62</b>	0.42
	Forces	6.2	<b>2.9</b>	3.7	2.6
Malonaldehyde	Energy	1.5	<b>1.1</b>	<b>1.1</b>	0.80
	Forces	10.2	<b>5.2</b>	6.6	4.6
Naphthalene	Energy	1.2	3.9	<b>0.46</b>	0.27
	Forces	6.5	<b>1.3</b>	2.6	1.5
Paracetamol	Energy	2.9	<b>1.3</b>	1.9	1.2
	Forces	12.2	<b>5.6</b>	7.1	4.5
Salicylic Acid	Energy	1.8	0.8	<b>0.73</b>	0.52
	Forces	9.5	4.1	<b>3.8</b>	2.9
Toluene	Energy	1.6	0.7	<b>0.45</b>	0.27
	Forces	8.8	<b>1.6</b>	2.5	1.6
Uracil	Energy	<b>0.6</b>	<b>0.6</b>	<b>0.58</b>	0.35
	Forces	4.2	<b>2.8</b>	3.8	2.4
Benzene	Energy	0.3	-	<b>0.07</b>	0.02
	Forces	2.6	-	<b>0.73</b>	0.27

### E.2 Inference timings

We report wall-clock timing results for evaluating the pretrained UNiTE model on dataset [44], all obtained using 16 cores of an Intel Xeon Gold 6130 CPU. We note that due to the Lagrangian formalism we have followed [65] to compute the analytic nuclear gradients in which the operator derivatives with respect to atomic coordinates do not need to be explicitly evaluated, the overhead for

computing energy and forces in addition to only computing the energies is still dominated by neural network back propagation.

Table E3: UNiTE energy calculation time breakdowns (mean/std in milliseconds) on benchmark [44].

Feature generation	NN inference
$85.8 \pm 40.1$	$181 \pm 83$

Table E4: UNiTE force calculation time breakdowns (mean/std in milliseconds) on benchmark [44].

NN back propagation	Nuclear gradient calculation
$273 \pm 7.3$	$33.2 \pm 1.8$

### E.3 Ablation studies

We perform ablation study to verify the effectiveness of our proposed normalization scheme, Equivariant Normalization (EvNorm). For baseline, we replace Equation 9 and Equation 11 with:

$$\mathbf{f}_u^t = \text{MLP}_1(\|\mathbf{h}_A^t\|) \odot \mathbf{h}_u^t \tag{E1}$$

$$\mathbf{h}_u^{t+1} = \mathbf{h}_u^t + \text{MLP}_2(\|\mathbf{q}_u\|) \odot \mathbf{q}_u \tag{E2}$$

which is similar to the ‘gated nonlinearity’ employed in some equivariant neural networks such as [2, 25]. Gated nonlinearity also preserves equivariance, but do not enforce constraints on the scale of the vector outputs. As shown in Table E5, using EvNorm clearly improves generalization on a representative task and is significantly more robust with respect to changing learning rates.

Table E5: Comparing EvNorm against a baseline, gated nonlinearity for learning  $U_0$  in QM9 with different learning rate setups for 300 epochs of training using Adam [74]. Statistics reported in the table indicates the prediction MAE (in meV) on the 10831-samples test set. FAIL indicates gradient explosion within training causing NaNs in the training loss.

Learning rate	Gated nonlinearity (baseline)	EvNorm (Ours)
5E-04	FAIL	3.5
3E-04	FAIL	3.6
1E-04	FAIL	3.4
5E-05	5.2	3.4
3E-05	6.5	3.3

### E.4 QM9 with uncertainty estimations

We provide the QM9 MAEs reported in Table 1 with additional confidence intervals for test errors, obtained by statistical bootstrapping with sample size 5000 and 100 iterations.

Table E6: QM9 statistics for UNiTE with 95% confidence intervals (CI) obtained by bootstrapping.

Target	Unit	Test MAE	Upper 95% CI	Lower 95% CI
$\mu$	mD	6.3	6.1	6.6
$\alpha$	$a_0^3$	0.036	0.034	0.038
$\epsilon_{\text{HOMO}}$	meV	9.9	9.5	10.1
$\epsilon_{\text{LUMO}}$	meV	12.7	12.4	13.0
$\Delta\epsilon$	meV	17.3	16.8	17.7
$\langle R^2 \rangle$	$a_0^2$	0.030	0.029	0.030
ZPVE	meV	1.11	1.06	1.14
$U_0$	meV	3.5	3.3	3.6
$U$	meV	3.5	3.4	3.6
$H$	meV	3.5	3.4	3.6
$G$	meV	5.2	5.0	5.3
$c_v$	$\frac{\text{cal}}{\text{molK}}$	0.022	0.0215	0.0225

## F Dataset and computational details

### F.1 Training datasets

The molecule datasets used in Section 5 are publicly accessible. The QM9 dataset [30] is released under the terms of Creative Commons Attribution 4.0 International (CC BY 4.0) license. The original MD17 dataset [38] is released under the terms of Creative Commons Attribution-NonCommercial 4.0 International (CC BY-NC 4.0) license and the Revised MD17 dataset [39] is released under the terms of Creative Commons Zero v1.0 Universal (CC0 1.0) license. The side-chain side-chain interaction (SSI) subset of the BioFragment Database (BFDdb) [41], which is referred to as BFDdb-SSI in Table 2, is accessed through the Quantum Chemistry Common Driver and Databases (QCDB) of Psi4 [78] which is released under the terms of GNU Lesser General Public License version 3 (LGPL-3.0) License. Following Section 2.1 of [42], the 2291 BFDdb-SSI samples for training and testing are selected as the sidechain-sidechain dimers in the original BFDdb-SSI dataset that are  $\leq 25$  atoms and do not contain sulfur element.

The dataset used for training the model described in Section 5.4 is collected from several different sources. First 11,827 neutral SMILES strings were extracted from the ChEMBL database [79] which is released under the terms of Creative Commons Attribution-Share Alike 3.0 Unported (CC BY-SA 3.0) Licence. For each SMILES string, up to four conformers were generated by Entos Breeze, and optimized at the GFN1-xTB level.[66] Non-equilibrium geometries of the conformers were generated using either normal mode sampling[80] at 300K or *ab initio* molecular dynamics for 200fs at 500K in a ratio of 50%/50%, resulting in a total of 178,836 structures An additional number 2,549 SMILES string were extracted from ChEMBL, and random protonation states for these were selected using Dimorphite-DL,[81] as well as another 2,211 SMILES strings which were augmented by adding randomly selected salts from the from the list of common salts in the ChEMBL Structure Pipeline.[82]. For these two collections of modified ChEMBL SMILES strings, non-equilibrium geometries were created using the same protocol described earlier, resulting in 21,141 and 27,005 additional structures for the two sets, respectively. To avoid excessive bias towards the larger drug-like molecules from ChEMBL, a number of SMILES strings were enumerated using a list of common bonding patterns, resulting in around 45,000 strings, from which a 9,830 subset was randomly sampled for which conformers were generated through Entos Breeze. Lastly, to increase the accuracy for non-covalent interactions, the molecules in the SSI and JSCH-2005 datasets were added to the training data set well.[41, 83] In total, the data set consists of 237,298 geometries spanning the elements C, O, N, F, S, Cl, Br, I, P, Si, B, Na, K, Li, Ca, and Mg. For each geometry DFT single point energies were calculated on the dataset at the  $\omega$ B97X-D3/def2-TZVP level of theory in Entos Qcore version 0.8.17.[68, 84, 85] Lastly, we additionally filtered the geometries for which DFT calculation failed to converge or broken bonds between the equilibrium and non-equilibrium geometries are detected, resulting in 235,818 geometries used for training the model described in Section 5.4.

## F.2 Electronic structure computational details

The dipole moment labels  $\vec{\mu}$  for QM9 dataset used in Section 5.1 were calculated at the B3LYP level of DFT theory with def2-TZVP AO basis set to match the level of theory used for published QM9 labels, using Entos Qcore version 1.1.0 [68, 86, 87]. The electron density labels  $\rho(\vec{r})$  for QM9 and BFDb-SSI were computed at the  $\omega$ B97X-D3/def2-TZVP level of DFT theory using Def2-TZVP-JKFIT density fitting basis [88] for Coulomb and Exchange fitting, also as the electron charge density expansion basis  $\{\Phi^\rho\}$ . The density coefficients  $\mathbf{d}$  are calculated as

$$d_\gamma = \sum_{\xi} \sum_{\mu,\nu} ((\mathbf{S}^\rho)^{-1})_{\gamma\xi} S_{\mu\nu;\xi} P_{\mu\nu} \quad (\text{F1})$$

where  $\mu, \nu$  are AO basis indices,  $\xi, \gamma$  are density fitting basis indices. Note that  $\gamma$  stands for the combined index  $(A, \nu_A, l, m)$  in (B30).  $\mathbf{P}$  is the DFT AO density matrix,  $\mathbf{S}^\rho$  is the density fitting basis overlap matrix, and  $S_{\mu\nu;\xi}$  are 3-index overlap integrals between the AO basis and the density fitting basis  $\{\Phi^\rho\}$ .

## F.3 Down-stream benchmark dataset details

We benchmark UNiTE on a number of well-established benchmark datasets that are representative of a variety of chemical problems to which QM calculations are commonly applied. A common task in drug-discovery research—ranking of drug-molecule conformations—is benchmarked via the Hutchison dataset of conformers of 700 molecules.[44] This tests the ability of a model to tell low-energy conformations from conformations with a higher energy. Torsional profiles benchmark a model’s ability to describe the potential energy surface of intramolecular rotations, and are crucial in describing the barrier between different conformational states of a molecule. We benchmark UNiTE’s ability to accurately describe the energy barriers of such torsional profiles using the TorsionNet500 benchmark set, which is the most diverse benchmark set available for this problem.[46] For other properties, such as interaction energies and intra-molecular interactions, we use the two corresponding the meta-subsets of the General Thermochemistry, Kinetics, and Non-covalent Interactions (GMTKN55) collection of 55 benchmark set.[45] The accuracy of the energy surfaces was benchmarked by performing geometry optimizations. Following [65], we perform geometry optimizations on the ROT34 dataset of small organic molecules and the MCONF dataset of melatonin conformers [47, 48]. ANI-2x energy calculations were performed with the TorchANI [89] package and and geometry optimizations were performed with the geomeTRIC optimizer [90] with default settings.

## F.4 Summary statistics calculation

The standardized MAE and standardized log MAE for QM9 reported in Table 1 are computed following the Appendix C of [24]. For the mean  $L^1$  electronic density error over the test sets reported in Table 2, we use 291 dimers as the test set for the BFDb-SSI dataset, and 10000 molecules as the test set for the QM9 dataset, following literatures [42, 43]. We note that two baseline methods used slightly different normalizations conventions, (a) normalizing over the number of molecules in the test set [43] or (b) normalizing over the total number of electrons in the test set [42]. We found the mean errors computed using normalization (b) is higher than (a) by  $\sim 5\%$  for our results. We exactly follow their individual definitions for mean  $L^1$  density errors for comparisons in Table 2, i.e. using scheme (a) in row 3 but scheme (b) in row 2.

The values summarized in Table 3 were calculated as described in this section. The task "Drug chemistry coverage" is calculated as the percentage of the molecules in the Hutchison conformers benchmark set which only contain elements and charge states which are supported by the ML or QM model. The "General chemistry coverage" metric is the percentage of subsets of the GMTKN55 benchmark set which only contain molecules for which the spin state, charge state, and element types which are supported by the ML or QM model. "Conformer ordering" is calculated as the median  $R^2$  correlation coefficient comparing the conformer energies from a given model to the energies from DLPNO-CCSD(T). In this task, the median  $R^2$  is calculated over the  $R^2$ -values for every molecule, and error bars are estimated by bootstrapping the pool of molecules. For torsion profiles, the mean absolute error of the predicted torsional barriers is calculated over all 500 molecules in the dataset. Again, error bars are estimated by bootstrapping in the pool of molecules. In the case of the reaction

energies and intra-molecular metasubsets of the GMTKN55 benchmark set collection, the updated weighted mean absolute deviation (WTMAD-2) is calculated as described in Ref. 45. For every ML or QM model, the WTMAD-2 is calculated over only the subsets of the two metasubsets for which every molecule is composed of only spin states, charge states, and element types which are supported by the ML or QM model. Error bars are obtained by bootstrapping within each subset and propagation of error is used to infer the corresponding error on the WTMAD-2 metric.

Geometry optimization accuracy is reported as the Cartesian root mean square deviation (RMSD) of the minimized geometry versus the reference level of theory ( $\omega$ B97X-D3/Def2-TZVP) averaged over molecules in the benchmark set. ANI-2x optimization failed on 19 out of 52 geometries on MCONF and 1 out of 12 geometries on ROT34, and the error is reported as “-”; on the subsets that ANI-2x geometry optimizations did not fail, the RMSD for ANI-2x is  $0.30\pm 0.02$  on MCONF and  $0.15\pm 0.04$  versus the reference level of theory.

## References

- [1] Michael M Bronstein, Joan Bruna, Taco Cohen, and Petar Veličković. Geometric deep learning: Grids, groups, graphs, geodesics, and gauges. *arXiv preprint arXiv:2104.13478*, 2021.
- [2] Nathaniel Thomas, Tess Smidt, Steven Kearnes, Lusann Yang, Li Li, Kai Kohlhoff, and Patrick Riley. Tensor field networks: Rotation-and translation-equivariant neural networks for 3d point clouds. *arXiv preprint arXiv:1802.08219*, 2018.
- [3] Taco Cohen and Max Welling. Group equivariant convolutional networks. In *International conference on machine learning*, pages 2990–2999. PMLR, 2016.
- [4] Pim de Haan, Maurice Weiler, Taco Cohen, and Max Welling. Gauge equivariant mesh cnns: Anisotropic convolutions on geometric graphs. *arXiv preprint arXiv:2003.05425*, 2020.
- [5] Robin Walters, Jinxi Li, and Rose Yu. Trajectory prediction using equivariant continuous convolution. *arXiv preprint arXiv:2010.11344*, 2020.
- [6] Gregor NC Simm, Robert Pinsler, Gábor Csányi, and José Miguel Hernández-Lobato. Symmetry-aware actor-critic for 3d molecular design. *arXiv preprint arXiv:2011.12747*, 2020.
- [7] Maurice Weiler, Mario Geiger, Max Welling, Wouter Boomsma, and Taco Cohen. 3d steerable cnns: Learning rotationally equivariant features in volumetric data. *arXiv preprint arXiv:1807.02547*, 2018.
- [8] Denis Boyda, Gurtej Kanwar, Sébastien Racanière, Danilo Jimenez Rezende, Michael S Albergo, Kyle Cranmer, Daniel C Hackett, and Phiala E Shanahan. Sampling using su (n) gauge equivariant flows. *Physical Review D*, 103(7):074504, 2021.
- [9] Ta-Pei Cheng and Ling-Fong Li. *Gauge theory of elementary particle physics*. Oxford university press, 1994.
- [10] Jun John Sakurai and Eugene D Commins. Modern quantum mechanics, revised edition, 1995.
- [11] Fabian B Fuchs, Daniel E Worrall, Volker Fischer, and Max Welling. Se (3)-transformers: 3d roto-translation equivariant attention networks. *arXiv preprint arXiv:2006.10503*, 2020.
- [12] Taco Cohen, Maurice Weiler, Berkay Kicanaoglu, and Max Welling. Gauge equivariant convolutional networks and the icosahedral cnn. In *International Conference on Machine Learning*, pages 1321–1330. PMLR, 2019.
- [13] Danilo Jimenez Rezende, George Papamakarios, Sébastien Racanière, Michael Albergo, Gurtej Kanwar, Phiala Shanahan, and Kyle Cranmer. Normalizing flows on tori and spheres. In *International Conference on Machine Learning*, pages 8083–8092. PMLR, 2020.
- [14] Thomas N. Kipf and Max Welling. Semi-Supervised Classification with Graph Convolutional Networks. In *International Conference on Learning Representations*, 2017. URL <https://openreview.net/forum?id=SJU4ayYgl>.

- [15] Justin Gilmer, Samuel S Schoenholz, Patrick F Riley, Oriol Vinyals, and George E Dahl. Neural message passing for quantum chemistry. In *Proceedings of the 34th International Conference on Machine Learning-Volume 70*, pages 1263–1272, 2017.
- [16] Yifan Feng, Haoxuan You, Zizhao Zhang, Rongrong Ji, and Yue Gao. Hypergraph neural networks. In *Proceedings of the AAAI Conference on Artificial Intelligence*, volume 33, pages 3558–3565, 2019.
- [17] Song Bai, Feihu Zhang, and Philip HS Torr. Hypergraph convolution and hypergraph attention. *Pattern Recognition*, 110:107637, 2021.
- [18] Victor Garcia Satorras, Emiel Hooeboom, and Max Welling. E (n) equivariant graph neural networks. *arXiv preprint arXiv:2102.09844*, 2021.
- [19] Brandon Anderson, Truong Son Hy, and Risi Kondor. Cormorant: Covariant molecular neural networks. In H. Wallach, H. Larochelle, A. Beygelzimer, F. d'Alché-Buc, E. Fox, and R. Garnett, editors, *Advances in Neural Information Processing Systems 32*, pages 14537–14546. Curran Associates, Inc., 2019. URL <http://papers.nips.cc/paper/9596-cormorant-covariant-molecular-neural-networks.pdf>.
- [20] Kristof T Schütt, Oliver T Unke, and Michael Gastegger. Equivariant message passing for the prediction of tensorial properties and molecular spectra. *arXiv preprint arXiv:2102.03150*, 2021.
- [21] Kristof Schütt, Pieter-Jan Kindermans, Huziel Enoc Saucedo Felix, Stefan Chmiela, Alexandre Tkatchenko, and Klaus-Robert Müller. Schnet: A continuous-filter convolutional neural network for modeling quantum interactions. In *Advances in neural information processing systems*, pages 991–1001, 2017.
- [22] Oliver T Unke and Markus Meuwly. Physnet: A neural network for predicting energies, forces, dipole moments, and partial charges. *J. Chem. Theory Comput.*, 15(6):3678–3693, 2019.
- [23] Ziteng Liu, Liqiang Lin, Qingqing Jia, Zheng Cheng, Yanyan Jiang, Yanwen Guo, and Jing Ma. Transferable multi-level attention neural network for accurate prediction of quantum chemistry properties via multi-task learning. *ChemRxiv*, 12588170:v1, 2020.
- [24] Johannes Klicpera, Janek Groß, and Stephan Günnemann. Directional message passing for molecular graphs. In *International Conference on Learning Representations (ICLR)*, 2020.
- [25] Simon Batzner, Tess E Smidt, Lixin Sun, Jonathan P Mailoa, Mordechai Kornbluth, Nicola Molinari, and Boris Kozinsky. Se (3)-equivariant graph neural networks for data-efficient and accurate interatomic potentials. *arXiv preprint arXiv:2101.03164*, 2021.
- [26] Yi Liu, Limei Wang, Meng Liu, Xuan Zhang, Bora Oztekin, and Shuiwang Ji. Spherical message passing for 3d graph networks. *arXiv preprint arXiv:2102.05013*, 2021.
- [27] Gurtej Kanwar, Michael S Albergo, Denis Boyda, Kyle Cranmer, Daniel C Hackett, Sébastien Racaniere, Danilo Jimenez Rezende, and Phiala E Shanahan. Equivariant flow-based sampling for lattice gauge theory. *Physical Review Letters*, 125(12):121601, 2020.
- [28] Sergey Ioffe and Christian Szegedy. Batch normalization: Accelerating deep network training by reducing internal covariate shift. In *International Conference on Machine Learning*, pages 448–456, 2015.
- [29] Jimmy Lei Ba, Jamie Ryan Kiros, and Geoffrey E Hinton. Layer normalization. *arXiv preprint arXiv:1607.06450*, 2016.
- [30] Raghunathan Ramakrishnan, Pavlo O Dral, Matthias Rupp, and O Anatole Von Lilienfeld. Quantum chemistry structures and properties of 134 kilo molecules. *Sci. Data*, 1(1):1–7, 2014.
- [31] Johannes Klicpera, Shankari Giri, Johannes T Margraf, and Stephan Günnemann. Fast and uncertainty-aware directional message passing for non-equilibrium molecules. *arXiv preprint arXiv:2011.14115*, 2020.

- [32] Bing Huang and O. Anatole von Lilienfeld. Quantum machine learning using atom-in-molecule-based fragments selected on the fly. *Nature Chemistry*, 12(10):945–951, September 2020. doi: 10.1038/s41557-020-0527-z. URL <https://doi.org/10.1038/s41557-020-0527-z>.
- [33] Felix A Faber, Anders S Christensen, Bing Huang, and O Anatole von Lilienfeld. Alchemical and structural distribution based representation for universal quantum machine learning. *J. Chem. Phys.*, 148(24):241717, 2018. doi: 10.1063/1.5020710.
- [34] Albert P Bartók, Sandip De, Carl Poelking, Noam Bernstein, James R Kermode, Gábor Csányi, and Michele Ceriotti. Machine learning unifies the modeling of materials and molecules. *Science advances*, 3(12):e1701816, 2017.
- [35] Zhuoran Qiao, Matthew Welborn, Animashree Anandkumar, Frederick R Manby, and Thomas F Miller III. Orbnet: Deep learning for quantum chemistry using symmetry-adapted atomic-orbital features. *The Journal of Chemical Physics*, 153(12):124111, 2020.
- [36] Anders S Christensen, Felix A Faber, and O Anatole von Lilienfeld. Operators in quantum machine learning: Response properties in chemical space. *The Journal of chemical physics*, 150(6):064105, 2019.
- [37] Max Veit, David M Wilkins, Yang Yang, Robert A DiStasio Jr, and Michele Ceriotti. Predicting molecular dipole moments by combining atomic partial charges and atomic dipoles. *The Journal of Chemical Physics*, 153(2):024113, 2020.
- [38] Stefan Chmiela, Alexandre Tkatchenko, Huziel E Sauceda, Igor Poltavsky, Kristof T Schütt, and Klaus-Robert Müller. Machine learning of accurate energy-conserving molecular force fields. *Science advances*, 3(5):e1603015, 2017.
- [39] Anders S Christensen and O Anatole von Lilienfeld. On the role of gradients for machine learning of molecular energies and forces. *Machine Learning: Science and Technology*, 1(4): 045018, 2020.
- [40] Stefan Chmiela, Huziel E Sauceda, Klaus-Robert Müller, and Alexandre Tkatchenko. Towards exact molecular dynamics simulations with machine-learned force fields. *Nature communications*, 9(1):1–10, 2018.
- [41] Lori A. Burns, John C. Faver, Zheng Zheng, Michael S. Marshall, Daniel G. A. Smith, Kenno Vanommeslaeghe, Alexander D. MacKerell, Kenneth M. Merz, and C. David Sherrill. The BioFragment database (BFDb): An open-data platform for computational chemistry analysis of noncovalent interactions. *The Journal of Chemical Physics*, 147(16):161727, October 2017. doi: 10.1063/1.5001028. URL <https://doi.org/10.1063/1.5001028>.
- [42] Alberto Fabrizio, Andrea Grisafi, Benjamin Meyer, Michele Ceriotti, and Clemence Corminboeuf. Electron density learning of non-covalent systems. *Chemical science*, 10(41):9424–9432, 2019.
- [43] Peter Bjørn Jørgensen and Arghya Bhowmik. Deepdft: Neural message passing network for accurate charge density prediction. *arXiv preprint arXiv:2011.03346*, 2020.
- [44] Dakota Folmsbee and Geoffrey Hutchison. Assessing conformer energies using electronic structure and machine learning methods. *Int. J. Quantum Chem.*, page e26381, 2020. doi: 10.1002/qua.26381.
- [45] Lars Goerigk, Andreas Hansen, Christoph Bauer, Stephan Ehrlich, Asim Najibi, and Stefan Grimme. A look at the density functional theory zoo with the advanced gmtkn55 database for general main group thermochemistry, kinetics and noncovalent interactions. *Physical Chemistry Chemical Physics*, 19(48):32184–32215, 2017.
- [46] Brajesh Rai, Vishnu Sresht, Qingyi Yang, Rayomond J Unwalla, Meihua Tu, Alan M Mathiowetz, and Gregory A Bakken. Torsionnet: A deep neural network to rapidly predict small molecule torsion energy profiles with the accuracy of quantum mechanics. 2020.

- [47] Tobias Risthaus, Marc Steinmetz, and Stefan Grimme. Implementation of nuclear gradients of range-separated hybrid density functionals and benchmarking on rotational constants for organic molecules. *Journal of Computational Chemistry*, 35(20):1509–1516, 2014.
- [48] Uma R Fogueri, Sebastian Kozuch, Amir Karton, and Jan ML Martin. The melatonin conformer space: Benchmark and assessment of wave function and dft methods for a paradigmatic biological and pharmacological molecule. *The Journal of Physical Chemistry A*, 117(10):2269–2277, 2013.
- [49] Jan Gerit Brandenburg, Christoph Bannwarth, Andreas Hansen, and Stefan Grimme. B97-3c: A revised low-cost variant of the b97-d density functional method. *The Journal of chemical physics*, 148(6):064104, 2018.
- [50] Christoph Bannwarth, Sebastian Ehlert, and Stefan Grimme. GFN2-xTB — an accurate and broadly parametrized self-consistent tight-binding quantum chemical method with multipole electrostatics and density-dependent dispersion contributions. *J. Chem. Theory Comput.*, 15(3):1652–1671, 2019.
- [51] Christian Devereux, Justin S Smith, Kate K Davis, Kipton Barros, Roman Zubatyuk, Olexandr Isayev, and Adrian E Roitberg. Extending the applicability of the ani deep learning molecular potential to sulfur and halogens. *Journal of Chemical Theory and Computation*, 16(7):4192–4202, 2020.
- [52] Alexander I Molev. Gelfand-tsetlin bases for classical lie algebras. *arXiv preprint math/0211289*, 2002.
- [53] Brian C Hall. *Quantum theory for mathematicians*, volume 267. Springer, 2013.
- [54] WH Klink and T Ton-That. Multiplicity, invariants, and tensor product decompositions of compact groups. *Journal of Mathematical Physics*, 37(12):6468–6485, 1996.
- [55] William Fulton and Joe Harris. *Representation theory: a first course*, volume 129. Springer Science & Business Media, 2013.
- [56] Arne Alex, Matthias Kalus, Alan Huckleberry, and Jan von Delft. A numerical algorithm for the explicit calculation of  $su(n)$  and  $sl(n, c)$  clebsch–gordan coefficients. *Journal of Mathematical Physics*, 52(2):023507, 2011.
- [57] S Gliske, W Klink, and T Ton-That. Algorithms for computing  $u(n)$  clebsch gordan coefficients. *Acta Applicandae Mathematicae*, 95(1):51–72, 2007.
- [58] Leon Lang and Maurice Weiler. A wigner-eckart theorem for group equivariant convolution kernels. *arXiv preprint arXiv:2010.10952*, 2020.
- [59] David Young. *Computational chemistry: a practical guide for applying techniques to real world problems*. John Wiley & Sons, 2004.
- [60] Douglas R Hartree. The wave mechanics of an atom with a non-coulomb central field. part i. theory and methods. *Math. Proc. Camb. Philos. Soc.*, 1928.
- [61] Andrew R Leach and Andrew R Leach. *Molecular modelling: principles and applications*. Pearson education, 2001.
- [62] RHWJ Ditchfield, W J\_ Hehre, and John A Pople. Self-consistent molecular-orbital methods. ix. an extended gaussian-type basis for molecular-orbital studies of organic molecules. *The Journal of Chemical Physics*, 54(2):724–728, 1971.
- [63] Ansgar Schäfer, Hans Horn, and Reinhart Ahlrichs. Fully optimized contracted gaussian basis sets for atoms li to kr. *The Journal of Chemical Physics*, 97(4):2571–2577, 1992.
- [64] Thom H Dunning Jr. Gaussian basis sets for use in correlated molecular calculations. i. the atoms boron through neon and hydrogen. *The Journal of chemical physics*, 90(2):1007–1023, 1989.

- [65] Zhuoran Qiao, Feizhi Ding, Matthew Welborn, Peter J Bygrave, Daniel GA Smith, Animashree Anandkumar, Frederick R Manby, and Thomas F Miller III. Multi-task learning for electronic structure to predict and explore molecular potential energy surfaces. *arXiv preprint arXiv:2011.02680*, 2020.
- [66] Stefan Grimme, Christoph Bannwarth, and Philip Shushkov. A robust and accurate tight-binding quantum chemical method for structures, vibrational frequencies, and noncovalent interactions of large molecular systems parametrized for all spd-block elements ( $Z=1-86$ ). *J. Chem. Theory Comput.*, 13(5):1989–2009, 2017.
- [67] Thom H Dunning and P Jeffrey Hay. Gaussian basis sets for molecular calculations. In *Methods of electronic structure theory*, pages 1–27. Springer, 1977.
- [68] Frederick Manby, Thomas Miller, Peter Bygrave, Feizhi Ding, Thomas Dresselhaus, Fidel Batista-Romero, Alexander Buccheri, Callum Bungey, Sebastian Lee, Rocco Meli, Kaito Miyamoto, Casper Steinmann, Takashi Tsuchiya, Matthew Welborn, Timothy Wiles, and Zack Williams. entos: A Quantum Molecular Simulation Package. *ChemRxiv preprint 10.26434/chemrxiv.7762646.v2*, 2019. URL [https://chemrxiv.org/articles/entos\\_A\\_Quantum\\_Molecular\\_Simulation\\_Package/7762646](https://chemrxiv.org/articles/entos_A_Quantum_Molecular_Simulation_Package/7762646).
- [69] Weitao Yang and Wilfried J Mortier. The use of global and local molecular parameters for the analysis of the gas-phase basicity of amines. *Journal of the American Chemical Society*, 108(19):5708–5711, 1986.
- [70] Trygve Helgaker, Poul Jorgensen, and Jeppe Olsen. *Molecular electronic-structure theory*. John Wiley & Sons, 2014.
- [71] Miguel A Blanco, Manuel Flórez, and Margarita Bermejo. Evaluation of the rotation matrices in the basis of real spherical harmonics. *Journal of Molecular Structure: THEOCHEM*, 419(1-3):19–27, 1997.
- [72] Manzil Zaheer, Satwik Kottur, Siamak Ravanbakhsh, Barnabas Poczos, Russ R Salakhutdinov, and Alexander J Smola. Deep sets. In I. Guyon, U. V. Luxburg, S. Bengio, H. Wallach, R. Fergus, S. Vishwanathan, and R. Garnett, editors, *Advances in Neural Information Processing Systems*, volume 30. Curran Associates, Inc., 2017. URL <https://proceedings.neurips.cc/paper/2017/file/f22e4747da1aa27e363d86d40ff442fe-Paper.pdf>.
- [73] Prajit Ramachandran, Barret Zoph, and Quoc V Le. Searching for activation functions. *arXiv preprint arXiv:1710.05941*, 2017.
- [74] Diederik P Kingma and Jimmy Ba. Adam: A method for stochastic optimization. *arXiv preprint arXiv:1412.6980*, 2014.
- [75] Ross Girshick. Fast r-cnn. In *Proceedings of the IEEE international conference on computer vision*, pages 1440–1448, 2015.
- [76] Ilya Loshchilov and Frank Hutter. Sgdr: Stochastic gradient descent with warm restarts. *arXiv preprint arXiv:1608.03983*, 2016.
- [77] Andrea Grisafi, Alberto Fabrizio, Benjamin Meyer, David M. Wilkins, Clemence Corminboeuf, and Michele Ceriotti. Transferable machine-learning model of the electron density. *ACS Cent. Sci.*, 5(1):57–64, 2019.
- [78] Daniel G. A. Smith, Lori A. Burns, Andrew C. Simmonett, Robert M. Parrish, Matthew C. Schieber, Raimondas Galvelis, Peter Kraus, Holger Kruse, Roberto Di Remigio, Asem Alenaizan, Andrew M. James, Susi Lehtola, Jonathon P. Misiewicz, Maximilian Scheurer, Robert A. Shaw, Jeffrey B. Schriber, Yi Xie, Zachary L. Glick, Dominic A. Sirianni, Joseph Senan O’Brien, Jonathan M. Waldrop, Ashutosh Kumar, Edward G. Hohenstein, Benjamin P. Pritchard, Bernard R. Brooks, Henry F. Schaefer, Alexander Yu. Sokolov, Konrad Patkowski, A. Eugene DePrince, Uğur Bozkaya, Rollin A. King, Francesco A. Evangelista, Justin M. Turney, T. Daniel Crawford, and C. David Sherrill. Psi4 1.4: Open-source software for high-throughput quantum chemistry. *J. Chem. Phys.*, 152(18):184108, 2020.

- [79] ChEMBL database release 27, May 2020. URL <https://doi.org/10.6019/chembl.database.27>.
- [80] Justin S. Smith, Olexandr Isayev, and Adrian E. Roitberg. ANI-1, a data set of 20 million calculated off-equilibrium conformations for organic molecules. *Scientific Data*, 4(1), December 2017. doi: 10.1038/sdata.2017.193. URL <https://doi.org/10.1038/sdata.2017.193>.
- [81] Patrick J. Ropp, Jesse C. Kaminsky, Sara Yablonski, and Jacob D. Durrant. Dimorphite-DL: an open-source program for enumerating the ionization states of drug-like small molecules. *Journal of Cheminformatics*, 11(1), February 2019. doi: 10.1186/s13321-019-0336-9. URL <https://doi.org/10.1186/s13321-019-0336-9>.
- [82] A. Patrícia Bento, Anne Hersey, Eloy Félix, Greg Landrum, Anna Gaulton, Francis Atkinson, Louisa J. Bellis, Marleen De Veij, and Andrew R. Leach. An open source chemical structure curation pipeline using RDKit. *Journal of Cheminformatics*, 12(1), September 2020. doi: 10.1186/s13321-020-00456-1. URL <https://doi.org/10.1186/s13321-020-00456-1>.
- [83] Petr Jurečka, Jiří Šponer, Jiří Černý, and Pavel Hobza. Benchmark database of accurate (MP2 and CCSD(t) complete basis set limit) interaction energies of small model complexes, DNA base pairs, and amino acid pairs. *Phys. Chem. Chem. Phys.*, 8(17):1985–1993, 2006. doi: 10.1039/b600027d. URL <https://doi.org/10.1039/b600027d>.
- [84] You-Sheng Lin, Guan-De Li, Shan-Ping Mao, and Jeng-Da Chai. Long-range corrected hybrid density functionals with improved dispersion corrections. *J. Chem. Theory Comput.*, 9(1): 263–272, 2013.
- [85] Florian Weigend and Reinhart Ahlrichs. Balanced basis sets of split valence, triple zeta valence and quadruple zeta valence quality for h to rn: Design and assessment of accuracy. *Physical Chemistry Chemical Physics*, 7(18):3297, 2005. doi: 10.1039/b508541a. URL <https://doi.org/10.1039/b508541a>.
- [86] Chengteh Lee, Weitao Yang, and Robert G Parr. Development of the Colle-Salvetti correlation-energy formula into a functional of the electron density. *Phys. Rev. B*, 37(2):785, 1988. doi: 10.1103/PhysRevB.37.785.
- [87] Florian Weigend and Reinhart Ahlrichs. Balanced basis sets of split valence, triple zeta valence and quadruple zeta valence quality for H to Rn: Design and assessment of accuracy. *Phys. Chem. Chem. Phys.*, 7, 2005.
- [88] Florian Weigend. Hartree–fock exchange fitting basis sets for h to rn. *Journal of computational chemistry*, 29(2):167–175, 2008.
- [89] Xiang Gao, Farhad Ramezanghorbani, Olexandr Isayev, Justin S Smith, and Adrian E Roitberg. Torchani: A free and open source pytorch-based deep learning implementation of the ani neural network potentials. *Journal of chemical information and modeling*, 60(7):3408–3415, 2020.
- [90] Lee-Ping Wang and Chenchen Song. Geometry optimization made simple with translation and rotation coordinates. *The Journal of chemical physics*, 144(21):214108, 2016.